

AD-A063 386

ARTEC ASSOCIATES INC HAYWARD CALIF
RESEARCH ON NON-IDEAL PLASMAS.(U)
JUL 78 D W BAUM, S P GILL, W L SHIMMIN

F/G 20/9

UNCLASSIFIED

FR-126

N00014-77-C-0463

NL

1 OF 2
AD
A063386

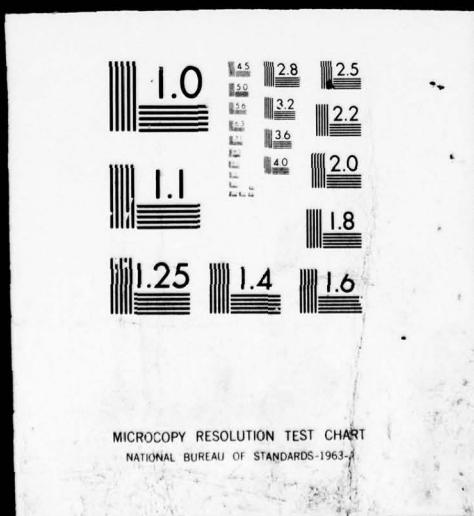


1

OF

2

AD
A063386



AD A063386

DDC FILE COPY

12

LEVEL

DISTRIBUTION STATEMENT A
Approved for public release
Distribution Unlimited

ARTEC 
ASSOCIATES INC

DDC

JAN 18 1979

A

79 01 04 014

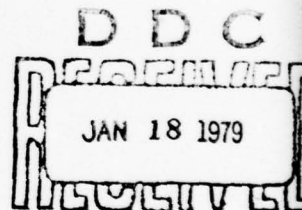
12

LEVEL #

RESEARCH ON NON-IDEAL PLASMAS

Final Report 126
Period: 25 May 1977 to
24 May 1978

Sponsored by: Office of Naval Research
Requisition Authority No.
NR 099-414/05-05-77 (473)
Contract No. N00014-77-C-0463



By: Dennis W. Baum, Stephen P. Gill,
W. Lee Shimmin, and D. Mukherjee

ARTEC ASSOCIATES INCORPORATED
26046 Eden Landing Road
Hayward, California 94545
Telephone: (415) 785-8080

DISTRIBUTION STATEMENT A
Approved for public release;
Distribution Unlimited

Reproduction in whole or in part is permitted for
any purpose of the United States Government.

79 01 04 014

UNCLASSIFIED

SECURITY CLASSIFICATION OF THIS PAGE (When Data Entered)

REPORT DOCUMENTATION PAGE		READ INSTRUCTIONS BEFORE COMPLETING FORM
1. REPORT NUMBER FR-126	2. GOVT ACCESSION NO.	3. RECIPIENT'S CATALOG NUMBER
4. TITLE (and Subtitle) RESEARCH ON NON-IDEAL PLASMAS.		5. TYPE OF REPORT & PERIOD COVERED Final Report 25 MAY 77 to 24 MAY 78
7. AUTHOR(s) D.W. Baum, S.P. Gill, W.L. Shimmin, and D. Mukherjee		6. PERFORMING ORG. REPORT NUMBER
9. PERFORMING ORGANIZATION NAME AND ADDRESS ARTEC ASSOCIATES INCORPORATED 26046 Eden Landing Road Hayward, CA 94545		8. CONTRACT OR GRANT NUMBER(s) N00014-77-C-0463
11. CONTROLLING OFFICE NAME AND ADDRESS Office of Naval Research, Dept. of Navy 800 N. Quincy St. CODE 613A:MS Arlington, VA 22217		10. PROGRAM ELEMENT, PROJECT, TASK AREA & WORK UNIT NUMBERS 61153N NR099-418 RR024-01-01
14. MONITORING AGENCY NAME & ADDRESS (if different from Controlling Office) 12 12 1 P.		12. REPORT DATE 24 July 1978
		13. NUMBER OF PAGES 119
16. DISTRIBUTION STATEMENT (of this Report) 16 RR 02401 17 RR 0240101		15. SECURITY CLASS. (of this report) UNCLASSIFIED
		15a. DECLASSIFICATION/DOWNGRADING SCHEDULE
17. DISTRIBUTION STATEMENT (of the abstract entered in Block 20, if different from Report) 10 Dennis W. /Baum, Stephen P. /Gill, W. Lee /Shimmin D. /Mukherjee		
18. SUPPLEMENTARY NOTES		
19. KEY WORDS (Continue on reverse side if necessary and identify by block number) Magnetohydrodynamics, Plasma, Energy Conversion, Explosive MHD, Explosive Driver		
20. ABSTRACT (Continue on reverse side if necessary and identify by block number) Research on advanced high performance explosive plasma sources for pulsed MHD power generators is reported.		

DISTRIBUTION STATEMENT A

Approved for public release
Distribution Unlimited

408 3.96

DD FORM 1 JAN 73 1473

EDITION OF 1 NOV 68 IS OBSOLETE

-2-

UNCLASSIFIED

SECURITY CLASSIFICATION OF THIS PAGE (When Data Entered)

PREFACE

This work was sponsored by the Power Program of the Office of Naval Research with John Satkowski as technical monitor; his support, comments, and direction are gratefully acknowledged. The advice and support of Dr. E. Florance of the ONR Pasadena Office is also gratefully acknowledged.

ADDITIONAL TO	
NO	DATE DUE <input checked="" type="checkbox"/>
NO	DATE DUE <input type="checkbox"/>
NO	DATE DUE <input type="checkbox"/>
BY <i>Peter on file</i>	
BY <i>...</i>	
CONSECUTIVE / AVAILABILITY CODES	
NO	DATE DUE / SPECIAL
A	

TABLE OF CONTENTS

	<u>Page</u>
DD FORM 1473.	2
PREFACE	3
LIST OF FIGURES	5
LIST OF TABLES.	7
1. INTRODUCTION.	8
1.1 Explosive MHD Generators	8
1.2 Conditions for Self-Excitation	9
1.3 High Energy Explosive Plasma Sources	10
1.4 Dense Non-Ideal Plasma Theory.	11
2. EXPERIMENTAL RESEARCH ON EXPLOSIVE PLASMA SOURCES	13
2.1 Experiment Plan.	13
2.2 Plasma Diagnostic Techniques	16
2.3 Asymmetric Explosive Driver.	30
2.4 Symmetric Explosive Drivers: Descriptions and Comparisons	37
2.5 Descriptions and Comparisons of Diagnostic Layouts	42
2.6 Experimental Results	46
2.7 Experimental Observations.	62
3. THEORETICAL RESEARCH ON NON-IDEAL PLASMAS	69
3.1 Research Objectives.	69
3.2 Ideal and Non-Ideal Plasma Theory.	71
3.3 Computational Methods.	91
3.4 Argon Calculations	98
3.5 Xenon Calculations	106
4. RESULTS AND RECOMMENDATIONS	116
4.1 Program Accomplishments.	116
4.2 Recommendations.	117
REFERENCES.	118

LIST OF FIGURES

<u>Figure</u>		<u>Page</u>
2.1	Simplified Schematic of Faraday MHD Generator	17
2.2	Cross-Section of Velocity Gage	19
2.3	Cross-Section Showing Velocity Gage Electrodes	19
2.4	End View of Load Circuit Configuration	22
2.5	Illustration of Eddy Currents Arising in Plasma Flow Due to Magnetic Field Gradient	25
2.6	Conductivity Gage Laboratory Calibration Curve for Shot 126-3	27
2.7	Geometrical Layout of Optical Pyrometer	29
2.8	Single-Sided Phased Disc Driver, Shot 126-1	31
2.9	Layout of Diagnostics for Shot 126-1	33
2.10	Velocity Gage and Load Voltage Records for Shot 126-1	36
2.11	Two-Sided Unphased Disc Drivers, Shots 126-2 and -3	39
2.12	Two-Sided Phased Disc Driver, Shots 126-4 and -5	41
2.13	Layout of Diagnostics for Shots 126-2 and -3	43
2.14	Layout of Diagnostics for Shots 126-4 and -5	45
2.15	Velocity Gage No. 1 and Load No. 1 Monitor Records for Shot 126-2	48
2.16	Velocity Gages No. 2 and No. 3 and Load No. 2 Voltage Records for Shot 126-2	49
2.17	Velocity Gage Record of Plasma Flow Velocity History on Shot 126-2	50
2.18	Comparison of Velocity Gage Records for Velocity Gages 2 and 3 on Shot 126-2	50
2.19	Plasma Conductivity History Obtained from Plasma Resistance Measurement from Load 1 on Shot 126-2	52
2.20	Load No. 1 Monitor Records for Shot 126-3.	54
2.21	Velocity Gage No. 2, Load No. 2 Monitor, and Velocity Gage No. 3 Output Versus Time for Shot 126-3.	55
2.22	Conductivity Gage Output Versus Time for Shot 126-3	56
2.23	Velocity Gage Record of Plasma Flow Velocity History on Shot 126-3	57

List of Figures (continued)

<u>Figure</u>		<u>Page</u>
2.24	Plasma Conductivity History Obtained from Plasma Resistance Measurements and from Eddy Current Measurement on Shot 126-3.	57
2.25	Channel Plasma Diagnostic Records for Shot 126-5	59
2.26	Conductivity Gage No. 1 and No. 3 Records for Shot 126-5	60
2.27	Velocity Gage Record of Plasma Flow Velocity History on Shot 126-5.	61
2.28	Plasma Conductivity Histories Obtained from Plasma Resistance Measurement and from Eddy Current Measurements on Shot 126-5. . .	61
2.29	Influence of Bow Shock on Phased Driver Operation.	67
3.1a	Convention Used in Denoting Ionization Potential (I_m) and Cumulative Ionization Potential (E_o^m).	77
3.1b	Convention Used in Denoting Electronic Energy Level (E_k^m) of m-ion with Respect to Ground State of Neutral Atom and Electronic Energy Level of m-ion with Respect to Ground State of m-ion (w_k^m)	78
3.2	Argon: Lines of Constant Interaction Parameter, Quantum Collisional Effects Parameter (QNTM) and Electron Degeneracy Parameter (DGN)--Based on Debye-Huckel Thermodynamics (DHO)..	104
3.3	Argon: Mollier Chart for $\rho(\text{Mg}\cdot\text{m}^{-3})$, S/R and $h(\text{J/kg})$. Calculations Based on Modified Debye-Huckel Theory (DHO).	107
3.4	Argon: Mollier Chart for Electrical Conductivity Using Rogov's Asymptotic Expression and Debye-Huckel Thermodynamics (DHO)	108
3.5	Xenon, T=10eV: Dependence of INTPAR, $\sigma_R(\text{kS}\cdot\text{m}^{-1})$, $u(\text{km}\cdot\text{s}^{-1})$, DGN, γ and Z^2 on P_e	112
3.6	Xenon, T=10eV: Dependence of $\rho(\text{Mg}\cdot\text{m}^{-3})$, $N_e(\text{m}^{-3})$, $P(\text{Pa})$, and QNTM on P_e	113

LIST OF TABLES

<u>Table</u>		<u>Page</u>
2.1	Summary of Experiments Performed.	15
2.2	Summary of Shock Parameters	63
2.3	Summary of Plasma Parameters.	63
3.1	Ionization Potentials (I_m) and Energy Groups (eV) and Group Degeneracies Used in Equation of State Calcula- tions for Argon100
3.2	Ionization Potentials (I_m) and Energy Groups (eV) and Group Degeneracies Used in Calculation of Equation of State of Xenon.110
3.3	Ionization Potential I_m (eV) for Argon and Xenon114

1. INTRODUCTION

1.1 Explosive MHD Generators

Explosively driven MHD generators operate by using an intermediary gas to transform explosive energy to useful electrical output. Detonating explosive is used to shock-compress and energize argon or xenon gas to a dense, high temperature, electrically conducting plasma. When this plasma is passed through a magnetic field, electric power is generated.

Previous research (References 1.1 to 1.3) has demonstrated explosive MHD generation with both externally excited and self-excited magnetic field. The greatest research interest is in self-excited generators, because of the wide variety of important practical applications. A self-excited explosive MHD generator comprises an explosive plasma source, a small permanent magnet, and a small field coil. In operation the plasma passing through the initial magnetic field generates power, which is used to increase the magnetic field. The increased field increases the power output, and both field and output grow exponentially until choked flow conditions are achieved in the generator.

Average thermal power flow (Reference 1.1) in explosive plasma sources is on the order of 10^{11} watts. At choked flow conditions electric power extraction can be expected to exceed 10%, or 10^{10} watts (10 gigawatts), an enormous power level by

present-day standards. Even more impressive is the small physical size of the generator, typically weighing on the order of 10 kg. By any standard of comparison a self-excited MHD generator, if successful, would provide a revolutionary new source of pulsed electric power.

1.2 Conditions for Self-Excitation

Although research to date has demonstrated some degree of self-excitation in an explosive MHD generator, achieved field amplification has fallen short of what is required for choked flow conditions and maximum enthalpy extraction (Reference 1.3). Field amplification necessary to go from a permanent magnet field of about 0.1 Tesla to choke field of about 15 Tesla is 150, or about 44 dB. The best experimental performance to date is about 20 dB in a multi-stage device, or half the required amplification.

The plasma parameters most important to the self-excitation process are velocity and conductivity (Reference 1.3). For a given electrical and field coil geometry the field amplification rate is proportional to the difference between the feedback resistance, which is proportional to velocity, and circuit resistance, which is dominated by the plasma resistance and hence is inversely proportional to plasma conductivity.

The plasma parameters produced by existing explosive plasma sources are inadequate to provide the required field amplification in a self-excited generator. The primary problem has been the plasma resistance, which has been found to be substantially less than predictions due to non-ideal plasma effects. Early predictions were in the range 30-50 kS/m, more than adequate to yield the desired amplification. Measured values were typically 5 to 10 kS/m, which reduced the amplification rate sufficiently that choke conditions were not achieved in self-excited MHD generators.

Achieving the desired amplification in a self-excited generator requires increasing the plasma conductivity or the plasma velocity. Substantially increasing the plasma conductivity has proven experimentally impossible, and it is now believed that non-ideal plasma effects limit the achievable conductivity.

1.3 High Energy Explosive Plasma Sources

Plasma energy and flow velocity from an explosive plasma source may be increased by increasing the concentration of explosive energy. Plasma is energized in an explosive driver by means of a strong shock wave. In the simplest systems the explosive piston driving the shock travels at explosive detonation velocity (8.5 km/sec for Octol explosive). Shock velocity may be increased somewhat by

radial convergence in a disc driver, and in principle it could be increased without limit by geometric phasing of the detonation velocity.

The experimental objective of the present program was to conduct research on advanced high performance plasma sources which could achieve substantially higher plasma energies and flow velocities than have been attained previously. By increasing flow velocity it was expected that the self-excitation limits caused by the experimental values of conductivity could be overcome. Furthermore it was anticipated that a higher energy plasma will yield a higher conductivity, further improving the self-excitation performance.

High energy explosive plasma sources are complex devices, and the resulting plasma pulse tends to be peaked and strongly time-varying. This is in contrast to the linear, constant velocity plasma source used in earlier research (Reference 1.1). Theoretical predictions are consequently more difficult.

Experimental development of high energy explosive plasma diagnostic measurements are described in Section 2 below.

1.4 Dense Non-Ideal Plasma Theory

It was concluded in our earlier research on explosive plasma sources (Reference 1.1) that non-ideal effects play a

major role in affecting theoretical plasma properties, and that predictions of plasma parameters including these non-ideal effects brought the theory into much closer agreement with experiment.

Research into the theory of dense non-ideal plasmas was continued in the present program, and detailed state-of-the-art calculations were performed on argon and xenon. This theoretical research is reported in Section 3 below.

2. EXPERIMENTAL RESEARCH ON EXPLOSIVE PLASMA SOURCES

2.1 Experiment Plan

The primary objective of the experimental program was to extend the state of the art of explosive plasma sources. In particular, to satisfy the requirements of self-excited explosive MHD generators, the objective was to increase plasma flow velocity and conductivity as much as possible by increasing plasma energy density.

Plasma is energized in an explosive plasma source by a strong shock wave, so in order to increase plasma energy the driving shock velocity must be increased. Our plan for the present research program was to increase driver shock velocity by phasing detonation or impact velocity, and by radial convergence of the shock. In addition the background channel gas density was reduced to increase channel shock velocity.

When an explosive detonation front impinges on a plate at an angle, the point of contact moves at a phase velocity that may be considerably greater than the detonation velocity. When the detonation propagates tangential to the plate the phase velocity is equal to the detonation velocity, and as the angle increases the phase velocity increases, approaching infinite phase velocity for normal incidence on the plate. The impact point between two plates follows the phase velocity, and ideally the driver piston formed by the impact can be phased to an arbitrarily high velocity.

In practice the achievable increase in phase velocity is severely limited by problems associated with achieving a gas seal at the impact point. Material inhomogeneities, boundary layer phenomena, and plasma compression properties all have a demonstrable effect on limiting the performance of a high velocity phased explosive driver. Achieving peak performance is at present more of an art than a science.

High velocity, high performance explosively driven plasma sources are considerably more complicated than the unphased plasma sources previously reported. The plasma state is also more complex. Instead of a relatively simple, constant velocity energizing shock wave there is a variable phase velocity piston combined with radial convergence and stagnation yielding an extremely energetic but non-constant plasma state.

To diagnose the plasma conditions a channel was used at the exit of the driver with a stainless steel foil separating the driver gas from the background channel gas. The diagnostics used in the channel were essentially the same as those used the year before, namely, an MHD plasma velocity gage, an electrode-to-electrode plasma resistance measurement, an electrodeless conductivity gage utilizing magnetic pickup of eddy currents, and shock wave propagation velocity measurements.

A summary of experiments performed in the program, together with diagnostic coverage, is shown in Table 2.1.

TABLE 2.1

SUMMARY OF EXPERIMENTS PERFORMED

<u>Shot No.</u>	<u>Description</u>	<u>Nominal Piston Velocity (km/sec)</u>	<u>Nominal Driver Pressure (GPa)</u>	<u>Velocity Gages</u>	<u>Plasma Resistance</u>	<u>Conductivity Gages</u>	<u>Comments</u>
126-1	Asymmetric Phased Disc	16	1.15	xx	xx	x	Gas seal inadequate
126-2	Symmetric Disc	8.5	0.6	xx	xx	x	Aluminum flyer plates
126-3	Symmetric Disc	8.5	1.0	xx	xx	x	Steel flyer plates
126-4	Symmetric Phased Disc	12	1.2	xx	x	xxx	No channel data
126-5	Symmetric Phased Disc	12	1.6	xx	x	xxx	

2.2 Plasma Diagnostic Techniques

Diagnostic Channel

A one-inch diameter channel for plasma diagnostic measurements was used on all experiments. The channel material was Lexan (polycarbonate resin manufactured by General Electric Co.), a 25-mm inner diameter tube with a 3-mm wall thickness. To prevent significant wall motion due to internal pressures of up to 100 MPa during approximately 20 μ s of measurements the channel was cast in Hydrostone (a high density plaster, $\rho = 1.76 \text{ Mg/m}^3$). The 120 mm diameter casting provided inertial tamping and was used on all shots.

MHD Velocity Gage

The velocity gage is based on the principle of a Faraday generator (Figure 2.1). When a conducting gas (a plasma) passes through a transverse magnetic field, a voltage is produced. When the flow velocity, magnetic field, and pick-up electrodes are mutually orthogonal, the open circuit voltage (zero current) is given by

$$V = buB$$

where b is the interelectrode distance in meters, u is the velocity in m/s, and B is the magnetic field in tesla. With a known magnetic field and known electrode spacing the measured voltage provides the plasma velocity history by

$$u(t) = \frac{V(t)}{bB}$$

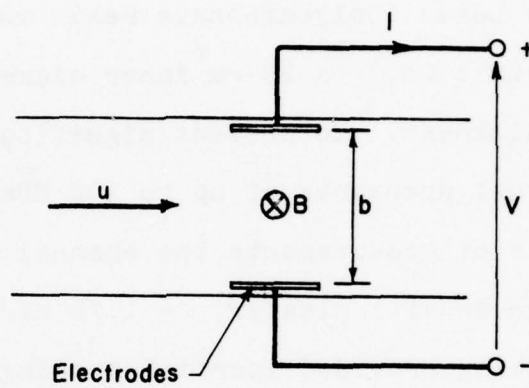


Figure 2.1 Simplified Schematic of Faraday MHD Generator

On all shots the transverse magnetic field was provided by a pair of barium ferrite magnets placed on either side of the channel (Figure 2.2) and cast in Hydrostone along with the channel. The magnets were 25 mm thick and 51 mm high and typically provided a field of approximately 0.1 tesla.

The electrodes consisted of 13 mm diameter threaded brass rods screwed into the Lexan tube and bonded and sealed in place with epoxy (Figure 2.3). The electrode surfaces had a 10° taper, and the leading edge was recessed 0.2 mm to minimize perturbation of the flow. Examination of the Lexan tubes after Shots 126-1 and -2 indicated that the electrodes were being rotated out of the flow by stagnation forces. Subsequently the portion of the electrodes outside the tube had 16 mm by 38 mm brass plates soldered to them to act as ballast in preventing the electrodes from being pushed out of the tube during the flow.

The electrodes were connected to a $50\ \Omega$ coaxial cable which went to an oscilloscope terminated in $50\ \Omega$. Since the plasma interelectrode resistance was $\lesssim 10\ \text{m}\Omega$, the $50\ \Omega$ termination was essentially an open circuit.

The velocity gage was calibrated in the laboratory by propelling a spring-driven aluminum rod through a mock-up of the velocity gage configuration. A dummy Lexan or glass tube served as the channel with the proper magnets positioned as on the shot. As the conductive aluminum rod passed through

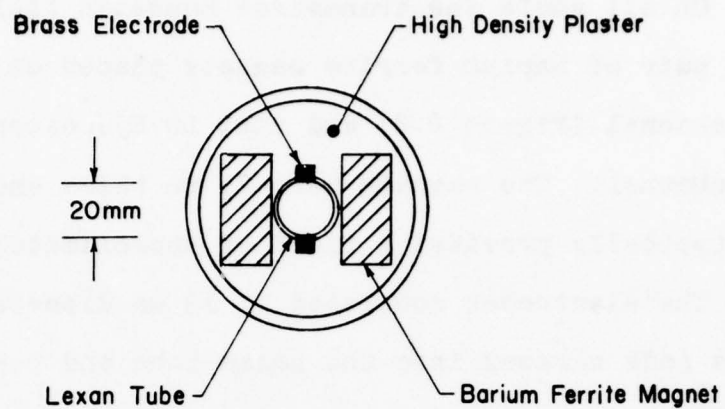


Figure 2.2 Cross-Section of Velocity Gage

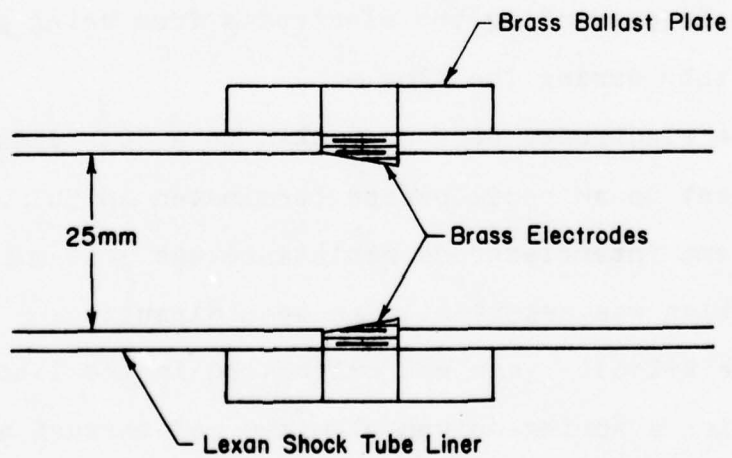


Figure 2.3 Cross-Section Showing Velocity Gage Electrodes

the magnetic field, a voltage was generated across the rod, proportional to the rod velocity, rod diameter, and effective magnetic field. Copper braid brush contacts were used to contact the rod and pick up the generated voltage.

The aluminum rod speed was monitored on each test using a collimated light source and a photodiode to record the arrival and departure of the rod at a given axial location. The rod deceleration was monitored using a pair of such setups at different locations. The measured deceleration of 35 m/s^2 amounted at most to a 2.5 percent correction to the measured average rod speed.

The calibrations were performed at rod speeds up to 10 m/s, and the effective B-fields were obtained from the measured output voltage and rod speed by

$$B_{\text{eff}} = \frac{V_{\text{out}}}{bu}$$

The output voltages were linear with rod speed in the range of the tests and proportional to the statically measured on-axis B-field, indicating that the measurements were not significantly affected by any eddy currents or skin depth problems.

Conductivity via Plasma Resistance Measurement

In addition to the velocity gage another Faraday generator was used in the channel to obtain the plasma resistance history and from that the effective plasma con-

ductivity. In this case the generator is provided with a 10 m Ω resistive load which approximately matches the expected plasma resistance.

The voltage appearing across the load electrodes equals the generator, or open circuit, voltage less the internal voltage drop:

$$V_L = V_0 - i R_i,$$

where i is the load circuit current and R_i is the plasma, or internal, resistance. The plasma inductive voltage drop, $L \frac{di}{dt}$, is negligible after one or two microseconds. The plasma resistance history can be obtained by measuring V_L , V_0 , and i .

The load consisted of a strip of stainless steel foil soldered to brass electrodes. The load inductance was typically around 25 nH. Figure 2.4 shows the load circuit arrangement including a search coil inductively coupled to the load to measure the load current. The load voltage is measured across the electrodes, and the open circuit voltage is obtained from the velocity gage record. Account must be taken of the time lag between the two diagnostic locations and differences in B-field amplitude, the load circuit typically having its own separate pair of barium ferrite magnets.

In order to relate the plasma resistance to the net, or effective, conductivity the gage factor for the particular electrode geometry was measured in the lab using a channel

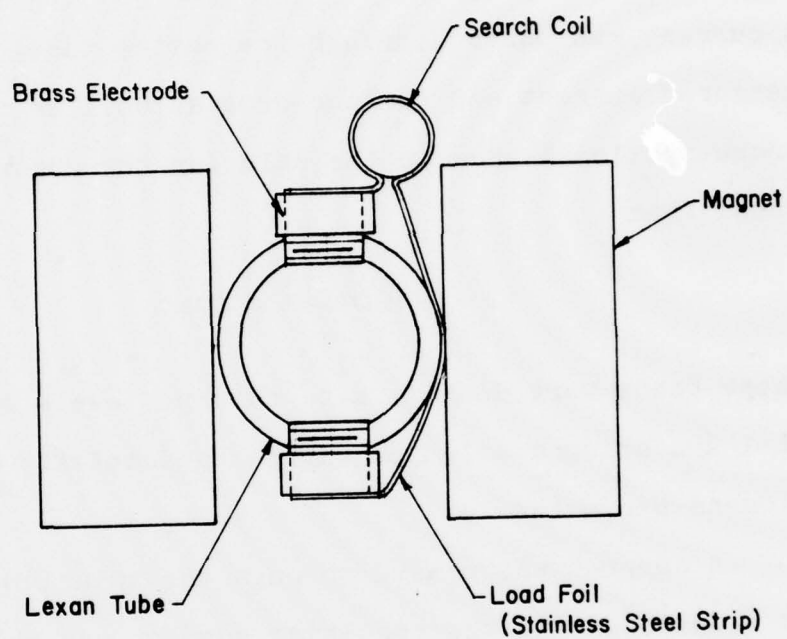


Figure 2.4 End View of Load Circuit Configuration

mock-up with copper electrodes and a solution of copper sulfate. To measure the conductivity of the solution the channel mock-up section was fitted with copper end plugs. A current was passed through the entire tube, and using the measured current and voltage drop as well as the length and cross-sectional area of the solution the conductivity was found from

$$\sigma = (I/R)(l/A) = (i/V)(l/A)$$

These tests were done at a.c. current levels of about 1 ampere at 1 kHz using a solution with a conductivity of about 2 siemens per meter.

A current was passed through the solution via the mock-up electrodes and the resulting current and voltage drop were measured. Using these measurements and the measured solution conductivity the geometry factor, or gage factor, is found as

$$\Gamma = R\sigma = (V/i)\sigma$$

For the electrode geometry used here the gage factor was determined to be 87.5 m^{-1} . The effective plasma conductivity on a shot was then calculated from

$$\sigma(t) = \Gamma/R_l = \Gamma i/(V_0 - V_L)$$

Conductivity via Eddy Current Measurement

When the plasma flows through an axial gradient in the B-field, there will likewise be an axial gradient in the MHD voltage, and this will result in circulating currents in the vicinity of the gradient as illustrated in Figure 2.5. A search coil placed outside the channel will have a voltage induced in it by the time variations in the magnetic fields produced by these eddy currents.

Output of the search coil is electronically integrated, so that it directly measures the field perturbation caused by the eddy currents:

$$V = NA \Delta B / \tau$$

where A is coil area, N is number of turns, and τ is the integrator time constant. The magnetic field perturbation ΔB is a function of magnetic Reynolds number, being theoretically linear with R_m at low values. Thus

$$\Delta B = f(R_m) = f(\mu_0 \sigma u b).$$

As with the velocity gage the conductivity gage is calibrated in the laboratory by propelling a spring-driven aluminum rod through a mock-up of the gage configuration. A dummy Lexan tube serves as the channel with the magnets and the search coil set up in the geometry to be used on the shot. Then the rod is propelled through the mock-up at different speeds and the integrated search coil output is measured.

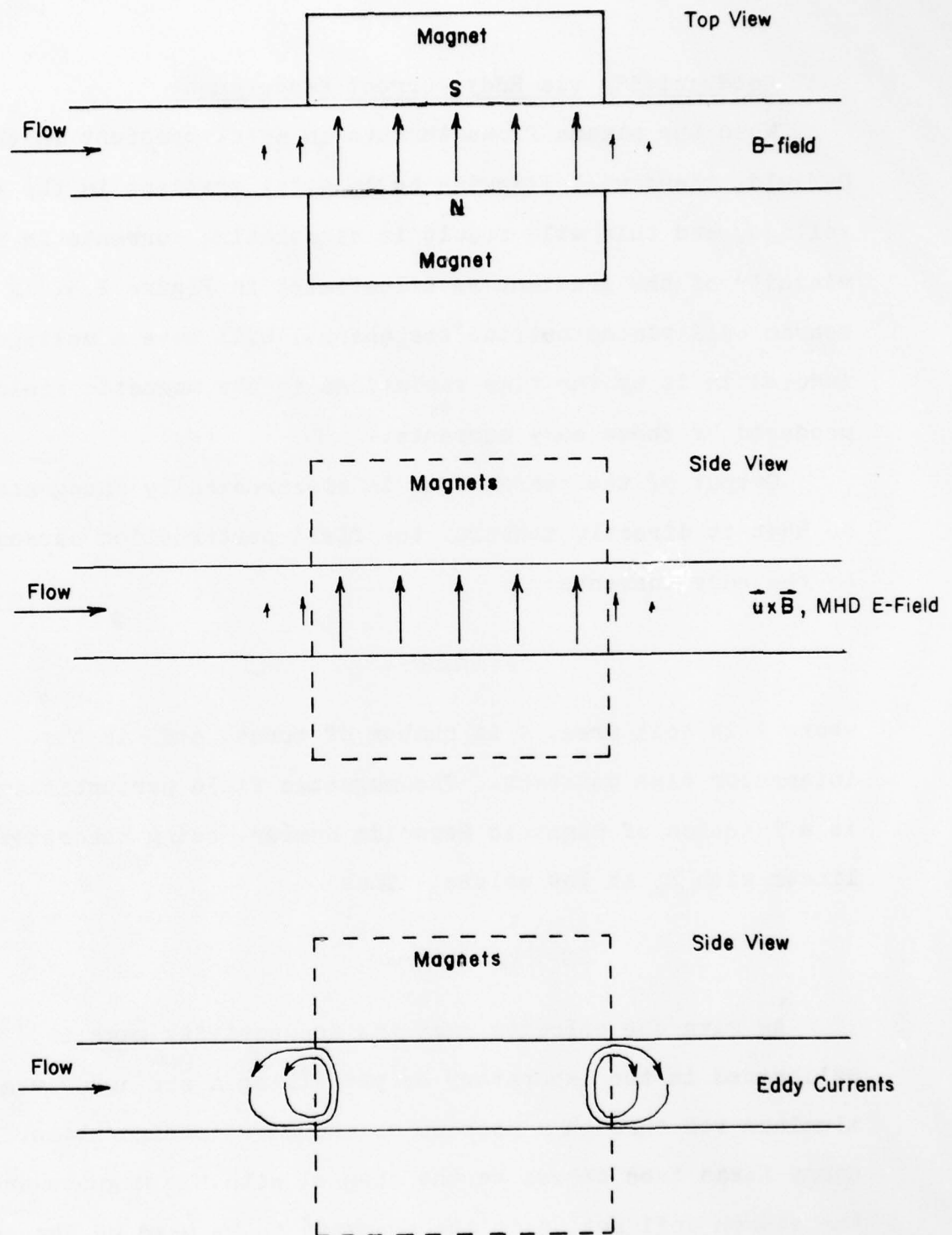


Figure 2.5 Illustration of Eddy Currents Arising in Plasma Flow Due to Magnetic Field Gradient

From the measured rod speed a plot is made of the search coil output versus rod speed (see the example in Figure 2.6).

Since there are several orders of magnitude difference between the laboratory rod velocities ($u_L \sim 10$ m/s) and the shot plasma flow velocities ($u_s \sim 10$ km/s), different time constant integrators are used in the two cases. From the signal level obtained on the shot the corresponding lab rod velocity is obtained from the plot using

$$u_L = u_L(V_L)$$

and

$$V_L \tau_L = V_s \tau_s$$

where the L suffix denotes a lab parameter and the S suffix denotes a shot parameter. The V's are integrated search coil output voltages, and the τ 's are integrator time constants.

Since the same output signal levels (i.e. V_τ) imply the same magnetic Reynolds number, or σu , the plasma conductivity is obtained from

$$\sigma_s = \frac{\sigma_L u_L}{u_s}$$

The shot flow velocity is obtained from the velocity gage record, and the aluminum rod conductivity is known to be 25 MS/m (type 6061 aluminum alloy). On Shots 126-4 and -5 a higher conductivity aluminum was used (type 1100 aluminum;

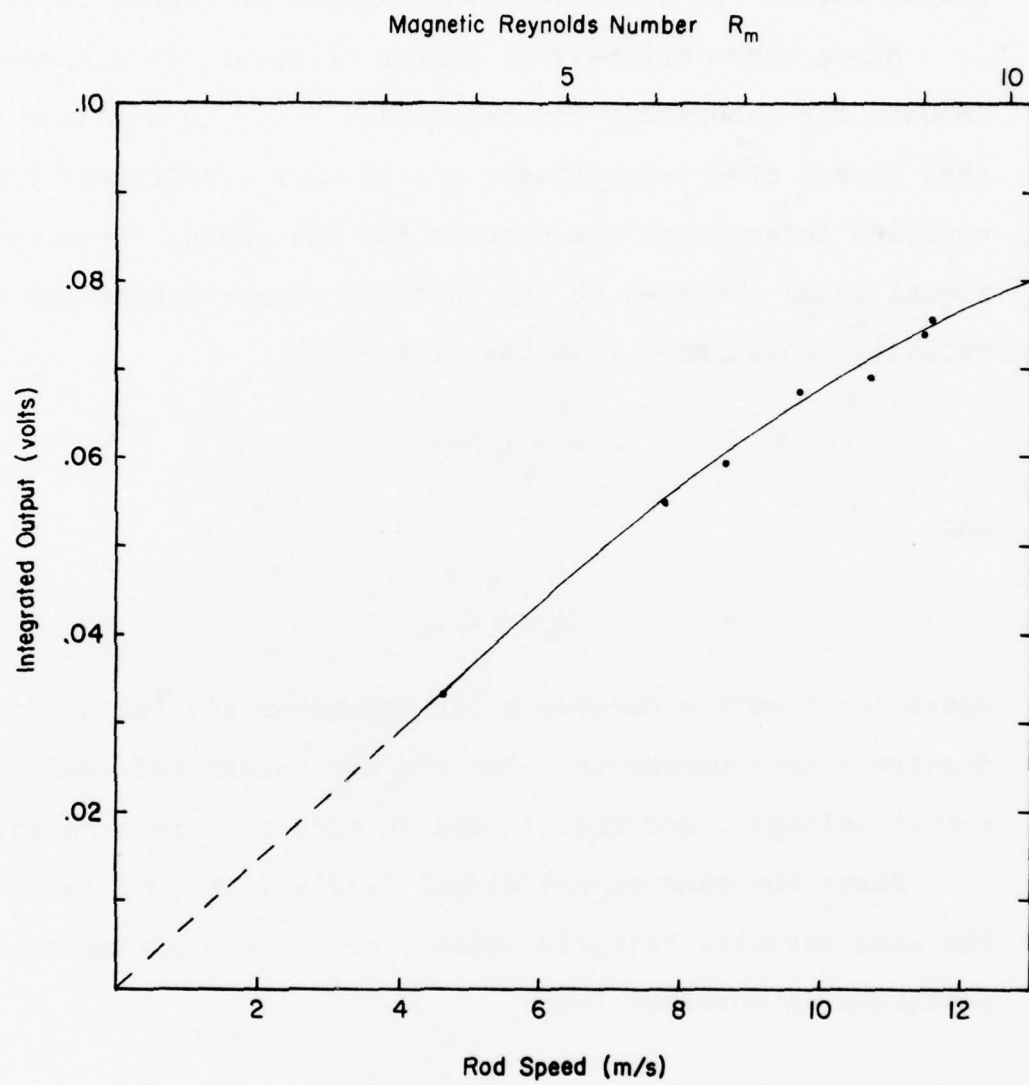


Figure 2.6 Conductivity Gage Laboratory Calibration Curve for Shot 126-3

$\sigma = 33 \text{ MS/m}$) to extend the range of the calibration to higher magnetic Reynolds number.

Optical Pyrometer

A simple expendable optical pyrometer was developed last year for measuring the plasma temperature. In the current effort the optical pyrometer was modified to the extent of using a different detector while using the same optical train. The geometrical layout of the device is shown in Figure 2.7. The device consists essentially of an aluminum housing, an optical train, and a silicon photodiode detector/operational amplifier combination. The optical train has a 0.343 mm diameter pinhole drilled in one-mil stainless steel, a steel aperture, a 9.0 nm width band-pass optical filter centered at 450 nm, and several pieces of Pyrex as fillers.

The detector used previously was an inexpensive, fast-rise phototransistor with high output signal level. Unfortunately accurate calibration was not possible because of the severe variation of sensitivity with angle of incidence. The detector used in the present work was a silicon photodiode operated in the photoconductive mode (PIN 5-D manufactured by United Detector Technology). While the photodiode does not have great angular variations in sensitivity, overall it is far less sensitive and requires an amplifier to provide a reasonable signal in a 50 Ω line. The amplifier used was the Model 201A also manufactured by United Detector Technology.

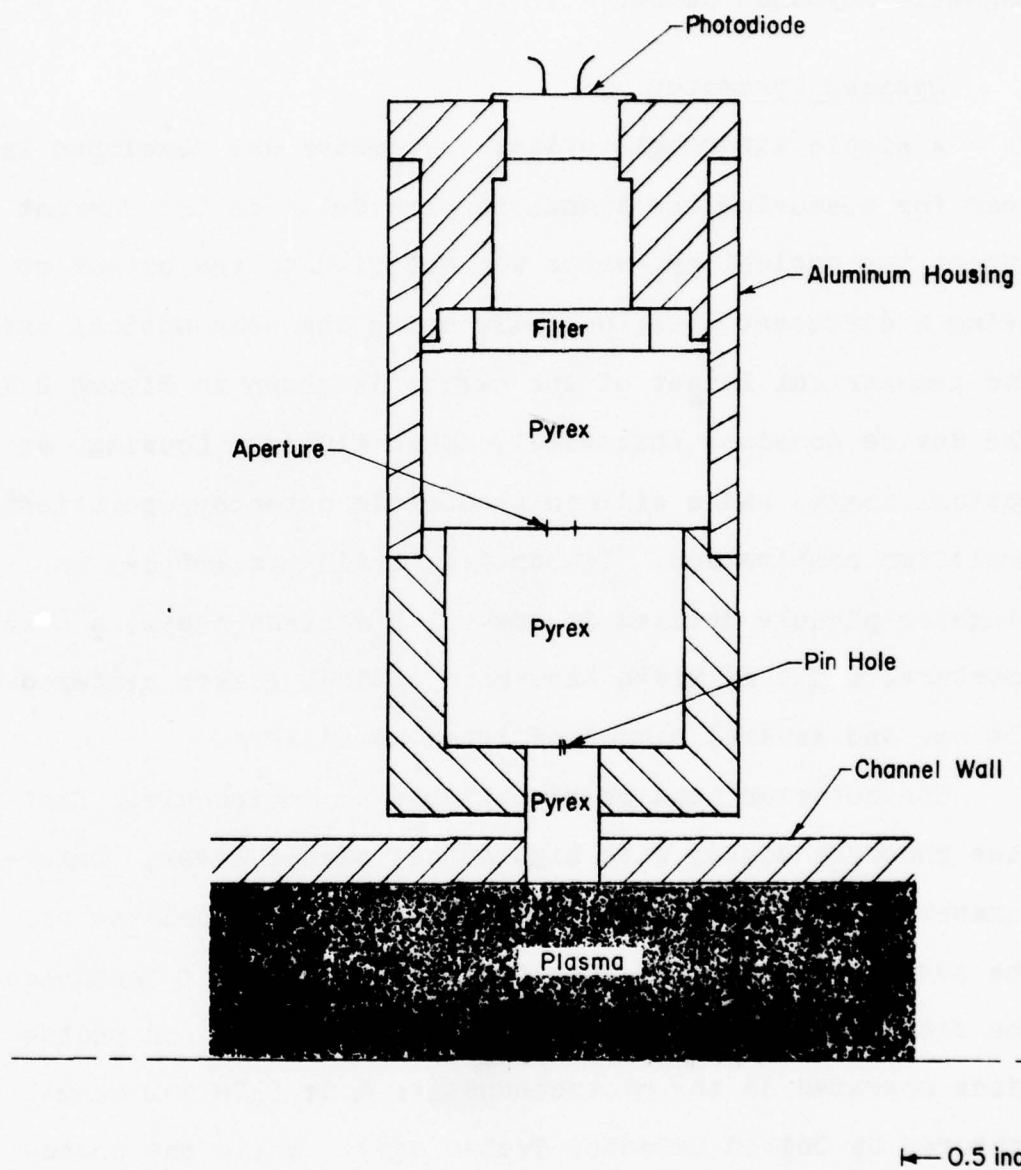


Figure 2.7 Geometrical Layout of Optical Pyrometer

For the initial work it was decided not to obtain absolute calibrations of the detector assemblies traceable to NBS radiation standards, but to proceed with the manufacturers' nominal sensitivities. The manufacturers' curves were used for both the transmission of the band-pass filters and for the spectral sensitivity of the PIN 5-D photodiodes. The transmissions of the Pyrex pieces at 450 nm were measured in the lab, and the pinhole diameters were measured in the lab with an optical comparator.

2.3 Asymmetric Explosive Driver

Driver Design

The first driver design tested in this program was a one-sided disc-type driver. A schematic of the driver is shown in Figure 2.8. The initiation scheme shown here was common to all disc drivers. It consists of a single detonator, a thin pad of explosive, and a wave shaper to provide shock isolation. This arrangement gives a symmetric and uniform ring-shaped detonation front as required for the operation of a disc driver.

In this case the wave shaper standoff from the steel flyer plate was adjusted so that the detonation front would impinge on the flyer plate at an angle of approximately 30° from normal incidence. The flyer plate is explosively accelerated and compresses the gas in the pressure chamber.

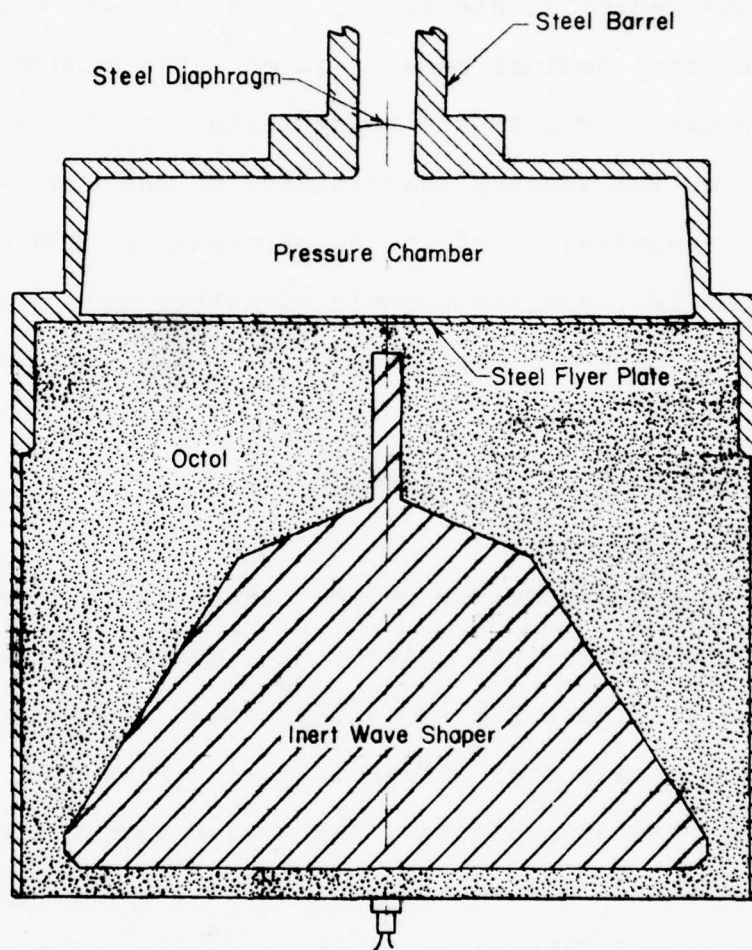


Figure 2.8 Single-Sided Phased Disc Driver, Shot 126-1

The flyer plate then impacts against the stationary front plate starting at the periphery. The impact progresses radially inward acting as a piston, converging the gas to stagnation at the axis.

Having the detonation front impinge on the flyer plate at 30° results in a radially inward sweep of the impact point at about 16 km/s. The internal energy density of a shock driven by such a piston is given by

$$e = \frac{1}{2} u^2$$

where u is the piston speed or particle flow speed. The piston speed would be the same as the detonation velocity (8.5 km/s for 75/25 Octol) for an unphased driver wherein the detonation propagates tangential to the flyer plate. Thus the phasing is roughly doubling the piston speed and hence increasing the energy density by a factor of four.

Diagnostic Layout

The layout for the diagnostics in the channel is shown in Figure 2.9. As indicated there are two velocity gage stations for obtaining plasma flow velocity histories and two load stations for obtaining the interelectrode resistance histories. There is a third pair of velocity gage electrodes further downstream with no magnets around them. These are intended as a noise check on the rest of the system.

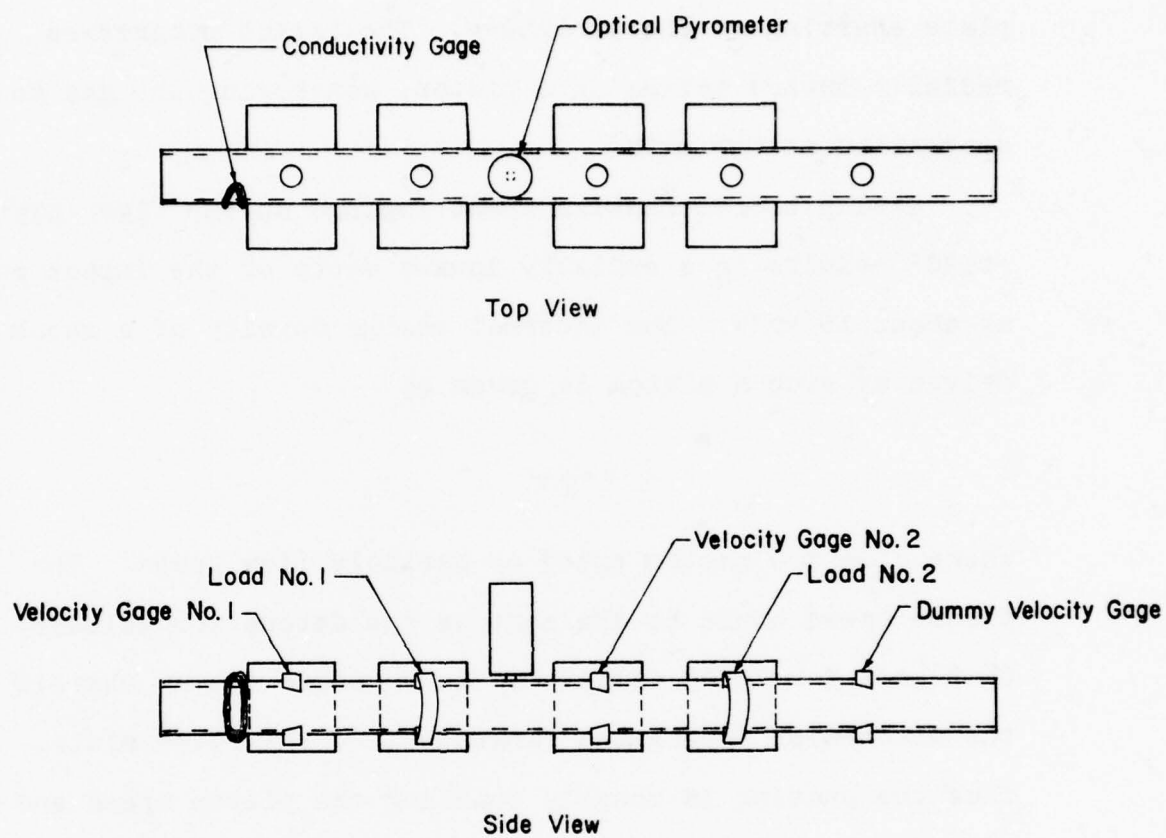


Figure 2.9 Layout of Diagnostics for Shot 126-1

The conductivity gage search coil is placed at the upstream edge (strong B-field gradient) of the first velocity gage magnets so that it is sufficiently far from the load to prevent spurious pickup due to currents flowing in the load. The optical pyrometer views the inside of the channel via a Pyrex rod which is glued into the channel wall to be flush with the channel wall inner surface.

On the driver self-shortening pins were placed on the periphery to monitor the location of the detonation front. Self-shortening pins were placed at the outer edge of the pressure chamber to monitor flyer plate motion. Self-shortening pins were also placed on the stationary plate to monitor the location of the inward-sweeping shock front. Finally a self-shortening pin was placed in the steel section of the channel to monitor shock arrival there. The pins were connected to a ladder network of R-C circuits, so that short-circuiting a pin generated a coded data point monitored on an oscilloscope.

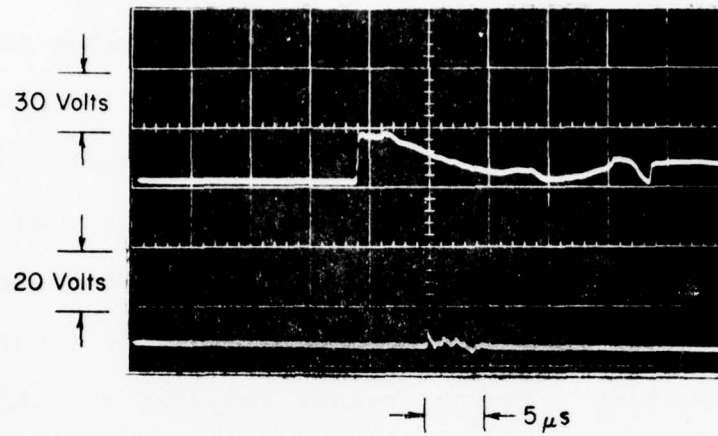
Experimental Results

From the pins on the pressure chamber it was observed that the symmetry was good, and the plate velocity was about 5 km/s. From the pin in the channel plus the shock arrival times at the various diagnostic stations in the channel it was determined that the channel shock speed was 13.1 km/s. A faulty trigger signal lead to an oscilloscope caused the remaining pin data to be lost.

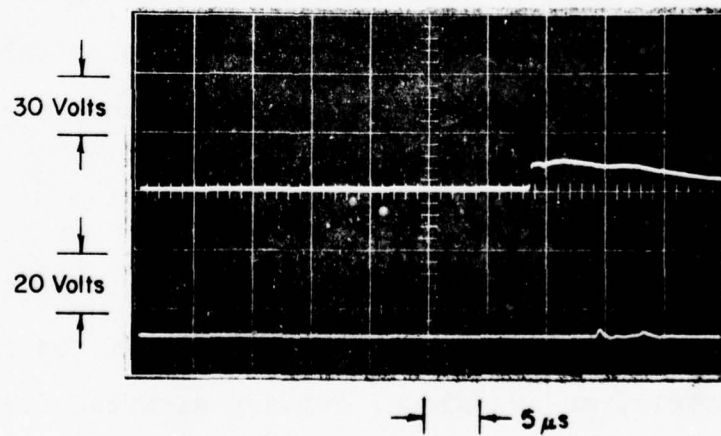
Scope records of the channel diagnostics are shown in Figure 2.10. The velocity gage and load voltage signals are in some cases distorted because of ground loops caused by some cable grounds inadvertently touching during the shot. The early part of Velocity Gage #1 is undisturbed, because the plasma is contacting only one pair of electrodes. Since there is no discontinuity in the velocity gage signal when the shock front arrives at Load #1, it can be presumed that the V.G. #1 and Load #1 grounds were not in contact. Therefore the first 15 μ s of the V.G. #1 signal is undistorted. After that time there is clearly a disturbance associated with shock front arrival at V.G. #2. The noise control station, V.G. #3 with no magnets, had no measurable signals, indicating that spurious plasma noise was not a problem in these measurements.

The velocity gage record indicates a short duration pulse (8 - 10 μ s) with an initial flow speed of 12.0 km/s. From the measured shock speed of 13.1 km/s in the channel air at approximately 1.3 kPa (10 Torr) the initial flow speed is calculated to be 12.2 km/s and the pressure, 2.4 MPa (24 bars). The agreement with the measured flow speed is well within the limits of error in the B-field measurement.

The load voltages and currents were much smaller than expected indicating a relatively high interelectrode resistance ($>200 \text{ m}\Omega$) and a correspondingly low conductivity ($<400 \text{ S/m}$). The conductivity gage did not show any measurable output.



a. Velocity Gage No.1 Output and Load No.1 Voltage Versus Time



b. Velocity Gage No.2 Output and Load No.2 Voltage Versus Time

Figure 2.10 Velocity Gage and Load Voltage Records for Shot 126-1

Significance of Results

The observed flow velocity was much less than anticipated. Detonation phase velocity was 16 km/s, and the flow velocity should have been at least this value or higher if the driver worked as expected.

It is now clear that the angle of impact of the flyer plate on the stationary plate was too shallow to form a proper gas seal. Consequently the gas in the periphery of the pressure chamber was not swept radially inward, and the only gas driven into the channel was that gas initially at or near the axis of the driver.

A calculation of the one-dimensional problem of a piston (speed, 5 km/s) driving a shock in xenon (initial density, 10.25 kg/m³) which then expands into air at 1.3 kPa gives an initial flow speed of 11.2 km/s and initial shock pressure of 2.0 MPa (20 bars). These values are close enough to the measured values to demonstrate the point that a gas seal was not achieved on this driver.

2.4 Symmetric Explosive Drivers: Descriptions and Comparisons

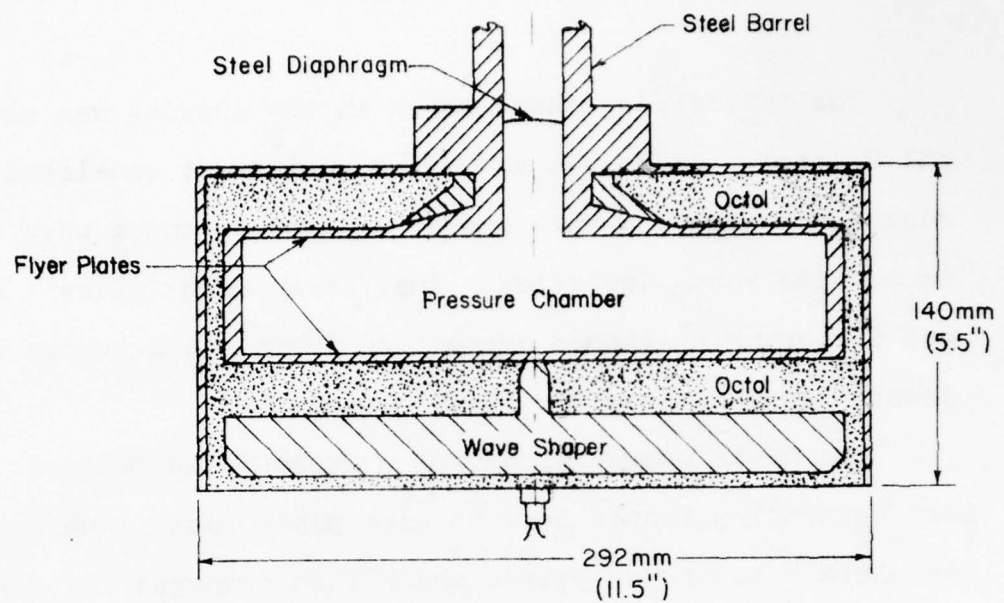
The drivers tested on the remainder of the program were all symmetric, or two-sided, drivers with two flyer plates driven together by two pads of explosive (see Figure 2.11a). This arrangement results in a higher impact pressure and gives a more reliable gas seal. The only disadvantage is that casting the explosive charge is more difficult in this geometry.

The initiation scheme shown in the drawing was used on all drivers. As on the asymmetric driver it consisted of a single detonator, a thin pad of explosive, and a wave shaper to provide shock isolation. This arrangement gives a symmetric and uniform ring-shaped detonation front which sweeps radially inward tangential to the flyer plates.

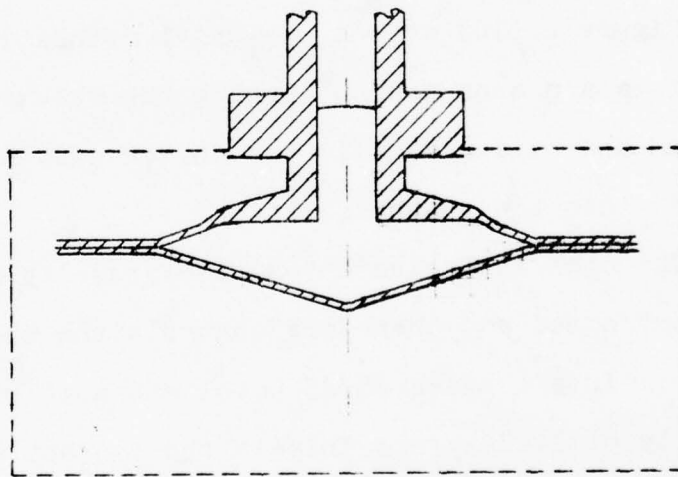
The basic operation of the drivers is as follows. As the detonation fronts next to each plate sweep inward they accelerate the flyer plates which then compress the gas ahead of them. The plates then impact against each other starting at the outer edge. The impact ring sweeps radially inward (see Figure 2.11b) at the explosive detonation velocity, acting as a piston and converging the shocked gas to stagnation at the axis. Finally the driver gas, now a plasma, re-expands into the channel.

The high explosive detonation velocity determines the "piston" speed and therefore controls the energetics of the driver. In all cases 75/25 Octol was used with a detonation velocity of 8.48 km/s. This is the fastest of the standard castable military explosives.

For the first test (Shot 126-2) in this series 3.2-mm-thick aluminum flyer plates were used with a charge-to-mass ratio of 5.0. This charge-to-mass ratio gives a high plate velocity (3.3 km/s) and a high impact angle (each plate, $\theta = 21^\circ$) to obtain a high impact pressure and assure a good gas seal. The initial density of the xenon driver gas was 7.4 kg/m^3 which



a. Disc Driver Before Firing



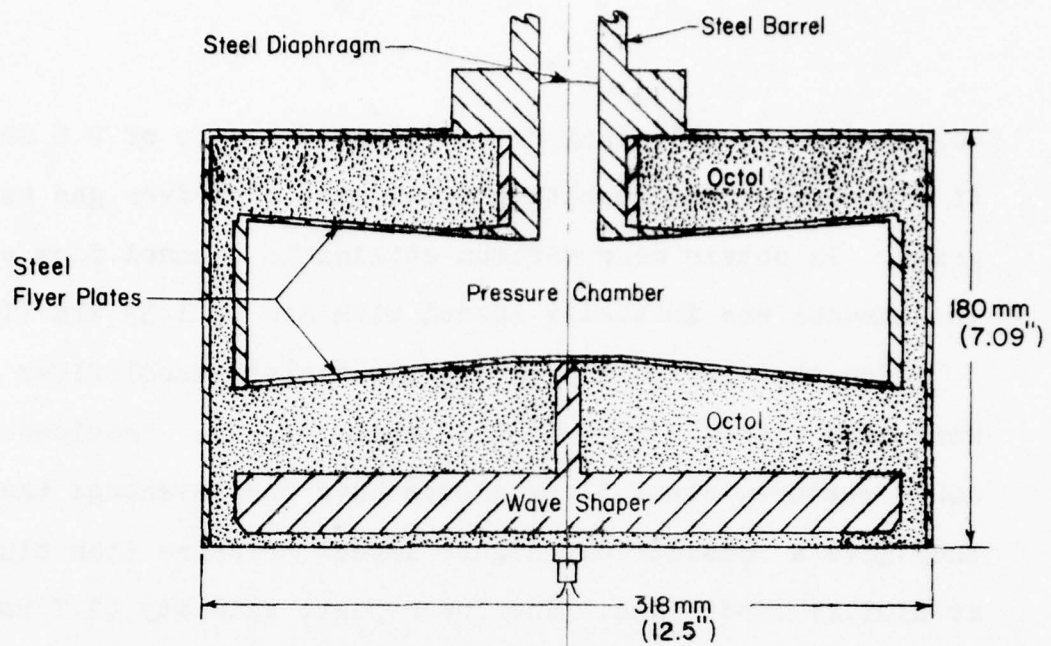
b. Disc Driver During Impact of Flyer Plates

Figure 2.11 Two-Sided Unphased Disc Drivers, Shots 126-2 and -3

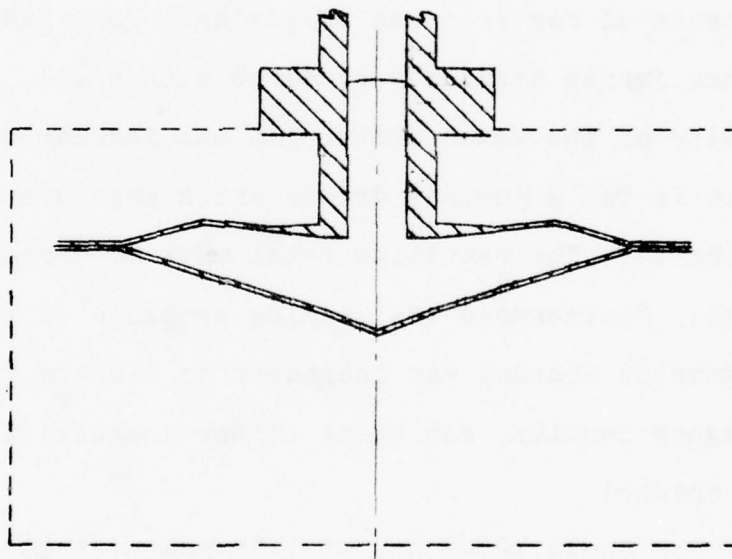
corresponds to a nominal driver shock pressure of 0.6 GPa (6 kilobars). The resulting total mass of driver gas was 19 grams. To obtain near maximum attainable channel flow speed the channel was initially loaded with air at 1.33 kPa (10 Torr).

For Shot 126-3 1.85-mm-thick stainless steel flyer plates were used with a charge-to-mass ratio of 2.9. Provided they don't rupture, steel flyer plates have the advantage that they give a considerably higher impact pressure than aluminum at similar conditions. The lower plate velocity (2.7 km/s) and lower impact angle (each plate, $\theta = 17.7^\circ$) are more than compensated for in terms of giving a good gas seal by the higher impact pressures obtained with steel. The initial density of the xenon driver gas was increased to 12.4 kg/m³ which is for a nominal driver shock pressure of 1.0 GPa (10 kilobars). The resulting total mass of driver gas was 31 grams. Furthermore the loading pressure of the air in the diagnostic channel was increased to 4.0 kPa (30 Torr) to give a higher density, and hence higher conductivity, plasma in the channel.

For Shots 126-4 and -5 1.85-mm-thick stainless steel flyer plates were again used. However, conical shaped rather than flat flyer plates were used (see Figure 2.12) to provide a phased impact. The plate angle (5.6°) was calculated to produce a radially inward moving plate impact of 12 km/s and thereby give a factor of two greater internal energy density in the shocked driver gas. To compensate for the reduction



a. Disc Driver Before Firing



b. Disc Driver During Impact of Flyer Plates

Figure 2.12 Two-Sided Phased Disc Driver, Shots 126-4 and -5

in impact angle due to the initial tilt the charge-to-mass ratio was increased, being now 4.5 at the outer edge and 5.9 near the axis. These give an impact angle for each plate of 20.7° at the outer edge increasing to 22.2° near the axis. To be certain of getting a good gas seal the xenon loading densities were decreased from that of Shot 126-3 to 7.4 kg/m^3 (28.1 grams total mass) on Shot 126-4 and 9.9 kg/m^3 (37.5 grams total mass) on Shot 126-5. These are for nominal driver shock pressures of 0.6 GPa (6 kilobars) and 0.8 GPa (8 kilobars) respectively. The diagnostic channels were again loaded with air at 4.0 kPa (30 Torr).

2.5 Descriptions and Comparisons of Diagnostic Layouts

The layout for the diagnostics in the channel on Shots 126-2 and -3 is shown in Figure 2.13. This layout is nearly the same as that of Shot 126-1 with two velocity gage stations, two load stations, a dummy velocity gage for looking at noise, one conductivity gage, and the optical pyrometer.

The modification to the layout consisted of placing the conductivity gage pickup coil downstream of the Velocity Gage #1 magnet and then reversing the positions of V.G. #1 and Load #1. The pickup coil was moved because it was found that the gage output is more nearly linear with increasing magnetic Reynolds number when the pickup coil is placed downstream from the B-field gradient. The diagnostic stations were then reversed to keep the pickup coil sufficiently distant from

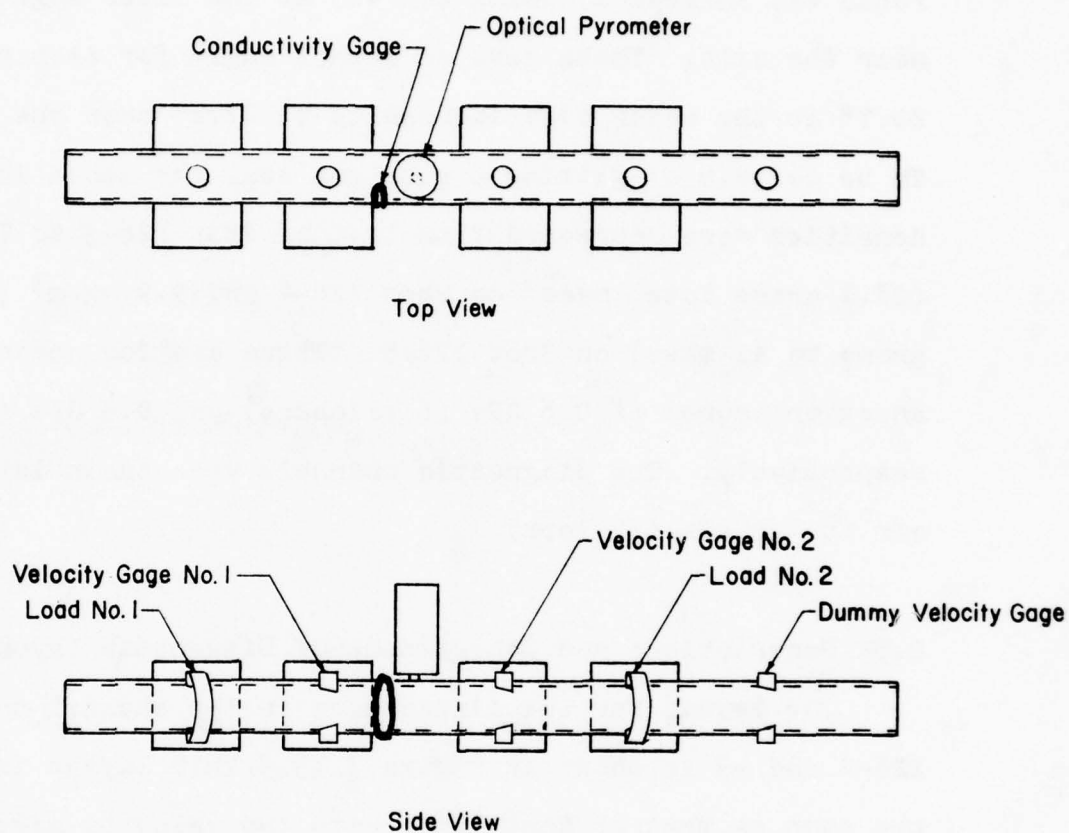


Figure 2.13 Layout of Diagnostics for Shots 126-2 and -3

the load to avoid spurious pickup due to currents flowing in the load.

Self-shorting pins were placed in various locations on the periphery of the driver to monitor the time-of-arrival of the detonation front in the high explosive. Since the pressure chambers were entirely surrounded with high explosive, pins could not be used to monitor flyer plate motion or shock transit in the driver gas.

The layout for the diagnostics in the channel on Shots 126-4 and -5 is shown in Figure 2.14. The principal change here is in using one pair of long magnets (305 mm) for the diagnostics rather than several pairs of shorter magnets.

Noisy signals have often been observed with velocity gages and load voltage measurements, particularly on shots with high conductivity and/or high flow speeds. In laboratory tests it was verified that sizeable signals are induced in these signal leads when there are nearby magnet field gradients and high magnetic Reynolds number flow ($R_m \geq 1$). The signal leads act as one-turn pickup coils which are sensitive to the time-varying B-fields associated with the eddy currents induced in the flowing plasma (or aluminum rod in the laboratory).

On these shots the signal leads were made as short as possible, and the axial magnetic field gradients were removed far (≥ 76 mm) from the diagnostic stations in order to decrease the spurious signals to acceptable levels. As indicated there were two velocity gage stations and one load station. The

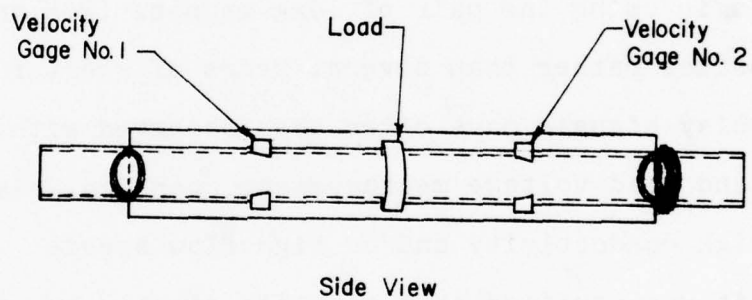
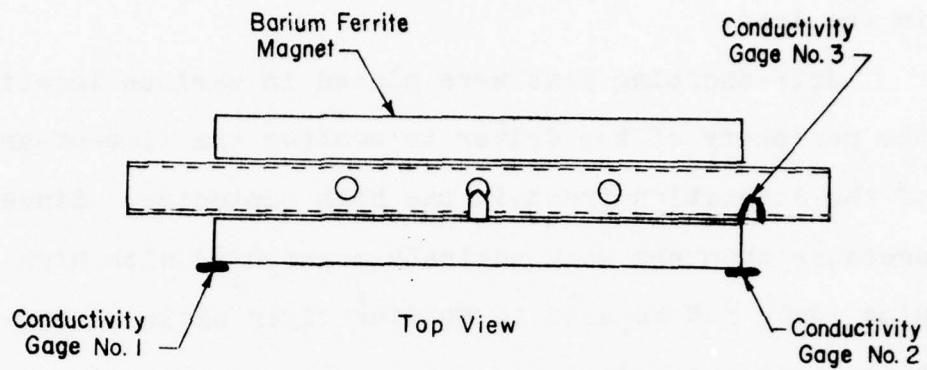


Figure 2.14 Layout of Diagnostics for Shots 126-4 and -5

optical pyrometer was not used on these shots.

There were three conductivity gages, one next to the channel (C.G. #3) and two placed outside the magnet and lined up centered on the magnet edge on each end as shown (C.G. #1 and #2). When the pickup coil is immediately adjacent to the plasma, then it is most sensitive to eddy currents flowing in the outer fringe of the plasma. If there are considerable variations in plasma conductivity across the plasma, the measured conductivity will be a weighted average biased toward the conductivity of the plasma at the near surface. In laboratory tests using a small current loop placed at various locations inside the channel it was found that somewhat better averaging of the conductivity could be obtained by moving the pickup coil farther from the channel. Thus the pickup coils were placed as indicated and calibrated in place. Conductivity Gage #3 was placed in the usual location to provide a comparison with C.G. #2 and as a reference for comparison with previous tests.

For these shots self-shortening pins were also placed in selected locations on the periphery of the drivers to monitor the time-of-arrival of the detonation front in the high explosive.

2.6 Experimental Results

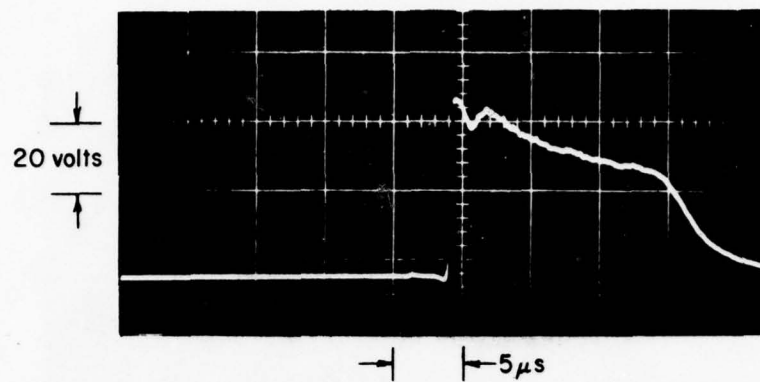
On Shots 126-2 through -5 the self-shortening pins on the drivers all reported, and in each case the detonation velocity was observed to be 8.5 km/s as expected. Furthermore the

azimuthal symmetry was observed to be excellent, the difference in time-of-arrival on the opposite sides of the driver being typically $0.2 \mu\text{s}$ or less.

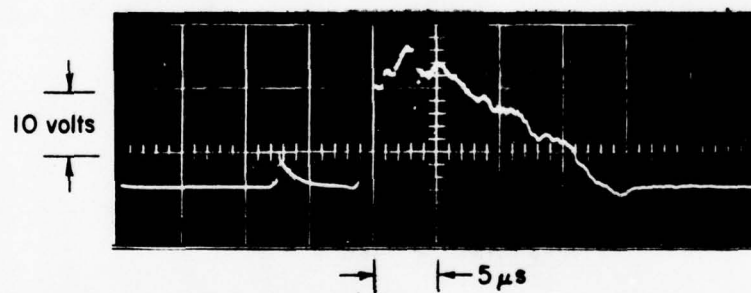
The scope records of the channel diagnostics on Shot 126-2 are shown in Figures 2.15 and 2.16. From shock arrival times at the diagnostic stations in the channel the shock speed was determined to be 23.6 km/s , and from the strong shock condition the calculated initial flow speed behind the shock is 21.6 km/s . The records from Velocity Gages #1 and #2 give initial flow speeds of 23.0 km/s and 20.2 km/s respectively, the first being 6.5% higher and the second being 6.5% lower than the calculated value based on the measured shock speed. Uncertainty in the effective B-field amounts to about 5%, and the uncertainty in the averaged electrode spacings is about 3%, so the measured flow speeds are correct within the limits of error of the velocity gage.

The flow speed histories from the two gages, normalized to the calculated initial flow speed of 21.6 km/s , are shown together in Figure 2.17. The pulse is approximately $17 \mu\text{s}$ in duration with an average flow speed of 16 km/s . The dip in the first few microseconds may be noise induced by eddy currents in the plasma.

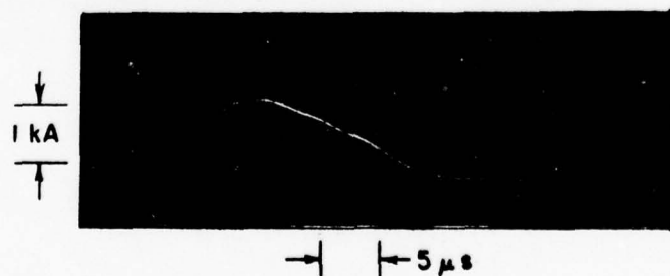
Velocity Gage #3, the noise check, has a small amplitude negative-going signal with noise superimposed on it. The negative signal is due to the return fields of the magnets upstream which are opposite to the main fields. A magnet



a. Velocity Gage No. 1 Output Versus Time

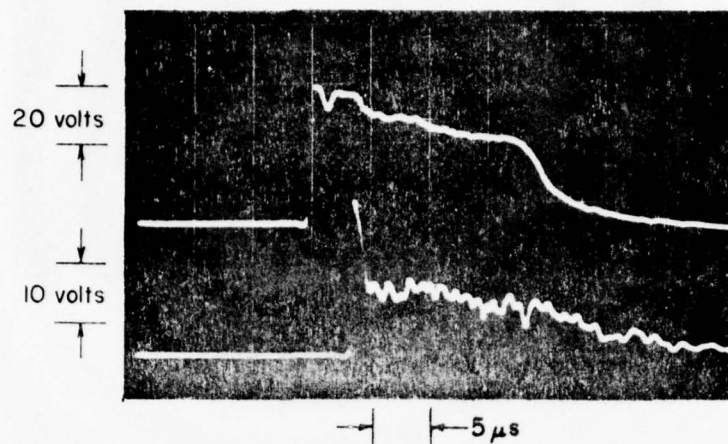


b. Load No. 1 Voltage Versus Time

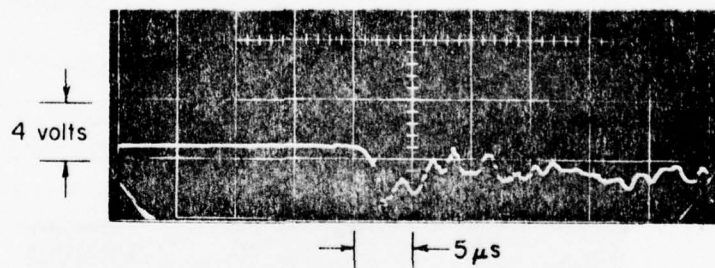


c. Load No. 1 Current Versus Time

Figure 2.15 Velocity Gage No. 1 and Load No. 1 Monitor Records for Shot 126-2



a. Velocity Gage No. 2 Output (Upper) and Load No. 2 Voltage (Lower) Versus Time



b. Velocity Gage No. 3 Output Versus Time

Figure 2.16 Velocity Gages No. 2 and No. 3 and Load No. 2 Voltage Records for Shot 126-2

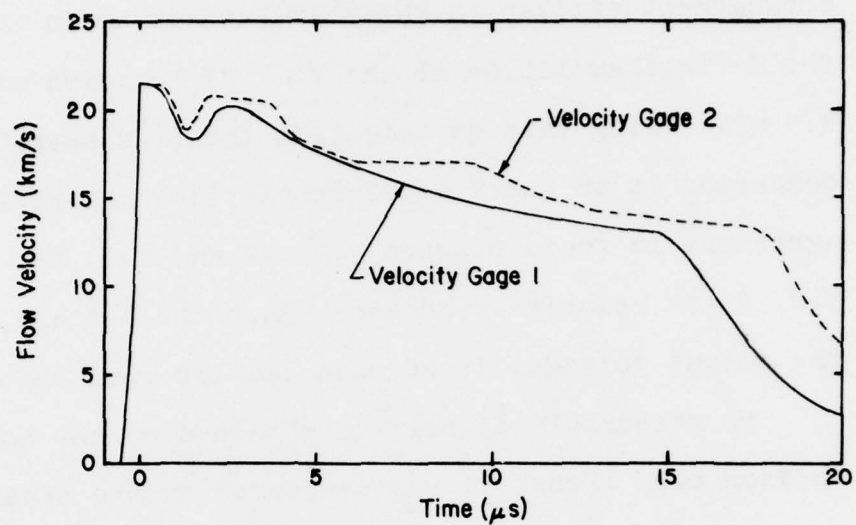


Figure 2.17 Velocity Gage Record of Plasma Flow Velocity History on Shot 126-2

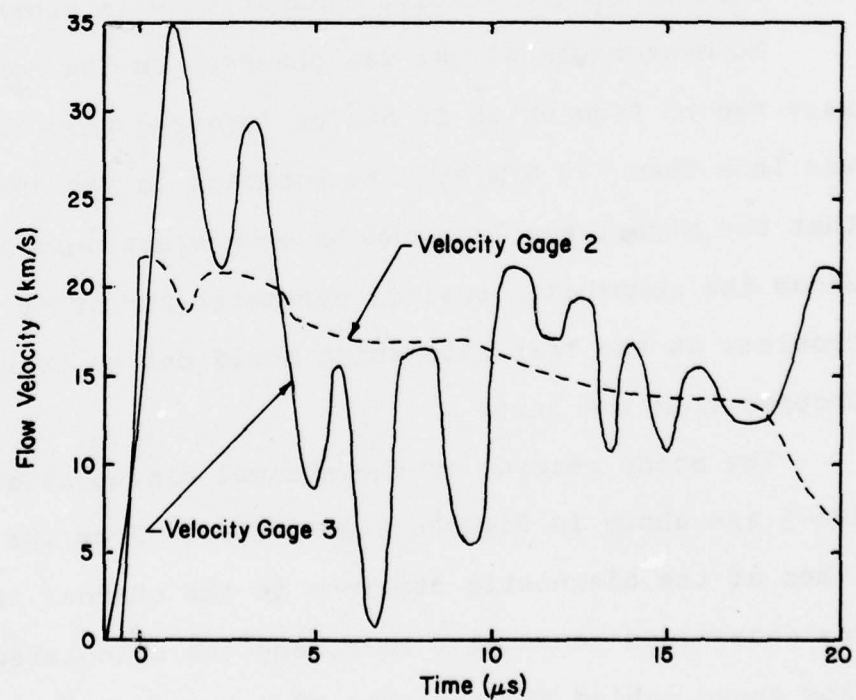


Figure 2.18 Comparison of Velocity Gage Records for Velocity Gages 2 and 3 on Shot 126-2

arrangement similar to the shot was set up in the lab and the B-field amplitude at the V.G. #3 location was found to be 4.5 mT. Using this to calculate the flow speed and then comparing it to the V.G. #2 result (see Figure 2.18) reasonable agreement is found between V.G. #2 and V.G. #3. The noise on V.G. #3 is relatively greater since the B-field, and hence the output voltage, is so much smaller than that of V.G. #2.

No measurable signal was obtained on the Load #2 current monitor even though it was monitored on two separate scopes. Furthermore the Load #2 Voltage waveform has an uncharacteristic shape and noise pattern. Load #1 has reasonable looking signals from which the plasma resistance history was obtained. The corresponding effective conductivity is shown in Figure 2.19.

No measurable signal was observed on the conductivity gage record from which it can be inferred that the conductivity was less than 440 S/m at that location in the channel or else that the signal was lost due to some electronic malfunction. Since the commercial optical pyrometer amplifier had noise problems at the test site which could not be traced, it was dropped from the test.

The scope records of the channel diagnostics on Shot 126-3 are shown in Figures 2.20 - 2.22. From the shock arrival times at the diagnostic stations in the channel the shock speed was determined to be 31.8 km/s, and the calculated initial flow speed behind the shock is 28.9 km/s. The Velocity Gage #1 record was lost, but the record from Velocity Gage #2 gives an

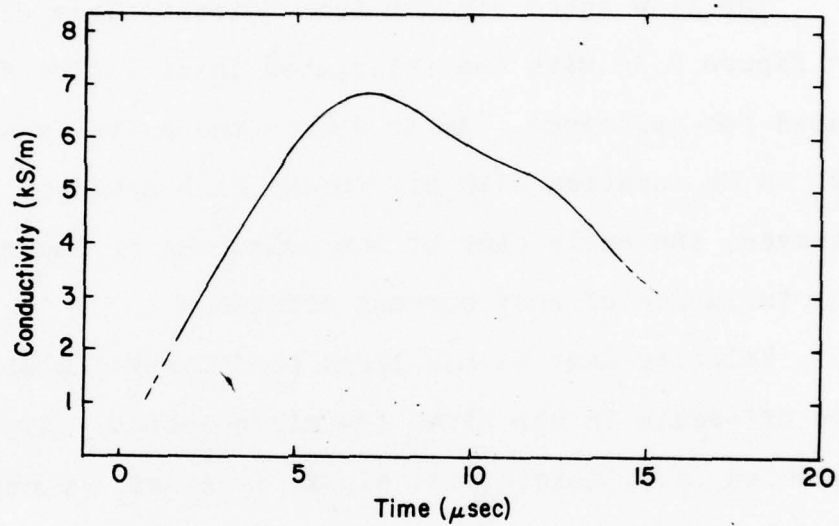


Figure 2.19 Plasma Conductivity History Obtained from Plasma Resistance Measurement from Load 1 on Shot 126-2

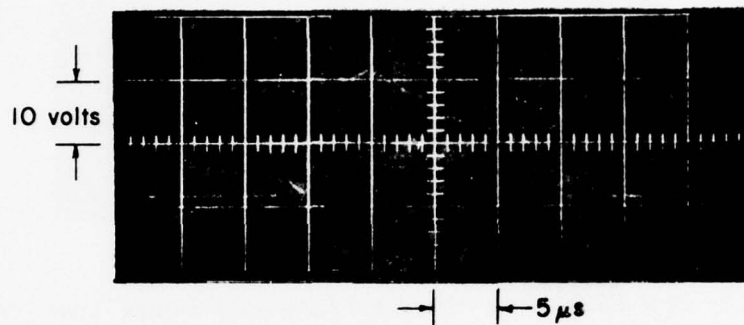
initial flow speed of 22.6 km/s which differs by 22% from the calculated value based on the measured shock speed. Uncertainty in the effective B-field amounts to about 5%, but eddy current effects, particularly stray coupling to the pick-up leads, may account for the discrepancy.

The flow speed history from Velocity Gage #2 is shown in Figure 2.23 with the calculated initial flow speed indicated for reference. As it stands the pulse is approximately 20 μ s in duration with an average flow speed of 14 km/s. However, the early part of the pulse may be incorrect due to the influence of eddy current effects.

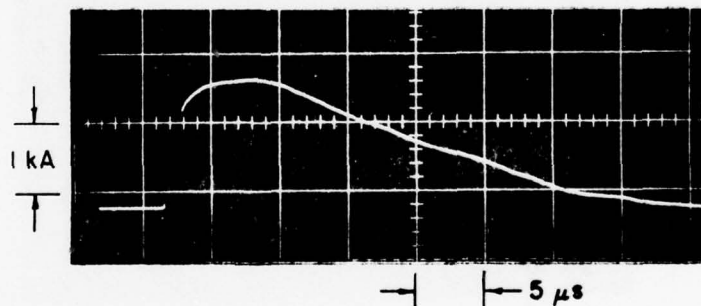
Velocity Gage #3 has large positive-going signals which are off-scale in the first few microseconds. Since the expected (i.e. noise-free) signal is a smaller negative signal, it is clear that the observed output is due to noise, presumably inductively coupled signals from eddy currents.

The current and voltage signals were obtained for both Load #1 and Load #2 and plasma resistance histories were obtained for both. Since no corrections were made for noise, these results are only provisional. The corresponding effective conductivity histories are shown in Figure 2.24 together with the conductivity history as obtained from the conductivity gage. At the highest conductivities the conductivity gage results are only approximate, having been extrapolated from the calibration curve.

The optical pyrometer amplifier was thoroughly checked

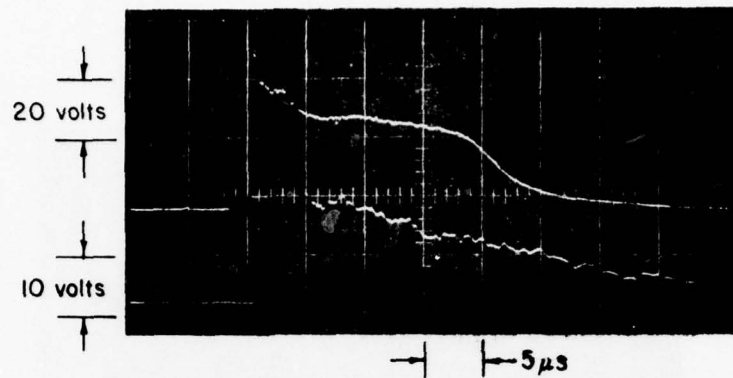


a. Load No. 1 Voltage Versus Time

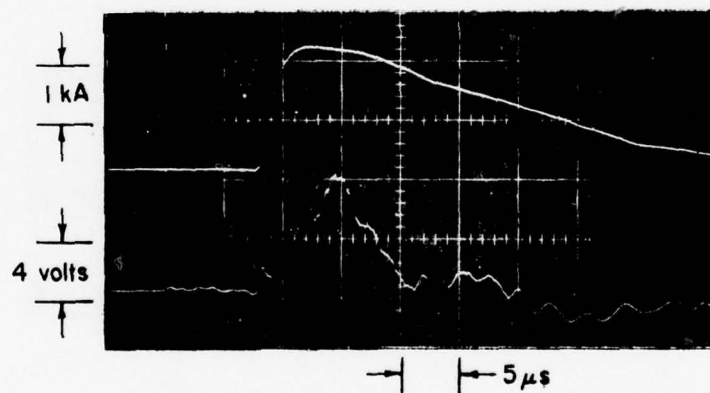


b. Load No. 1 Current Versus Time

Figure 2.20 Load No. 1 Monitor Records for Shot 126-3



a. Velocity Gage No. 2 Output (Upper) and Load No. 2 Voltage (Lower) Versus Time



b. Load No. 2 Current (Upper) and Velocity Gage No. 3 Output Versus Time

Figure 2.21 Velocity Gage No. 2, Load No. 2 Monitor, and Velocity Gage No. 3 Output Versus Time for Shot 126-3

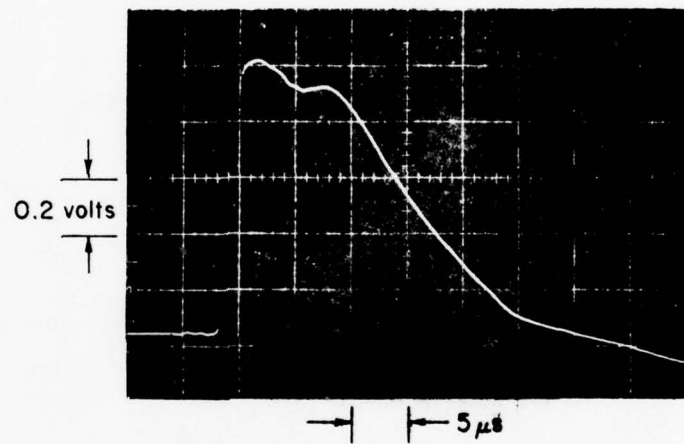


Figure 2.22 Conductivity Gage Output Versus Time for Shot 126-3

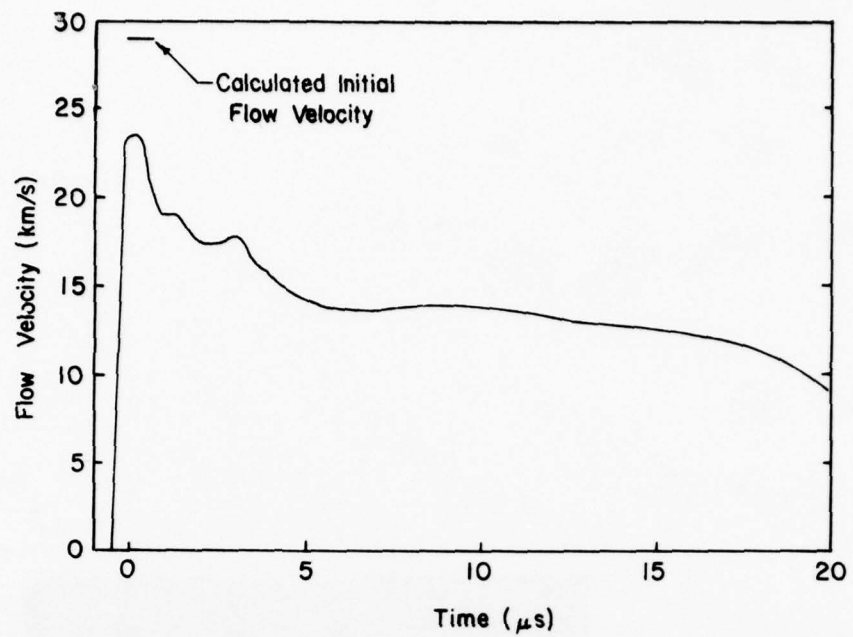


Figure 2.23 Velocity Gage Record of Plasma Flow Velocity History on Shot 126-3

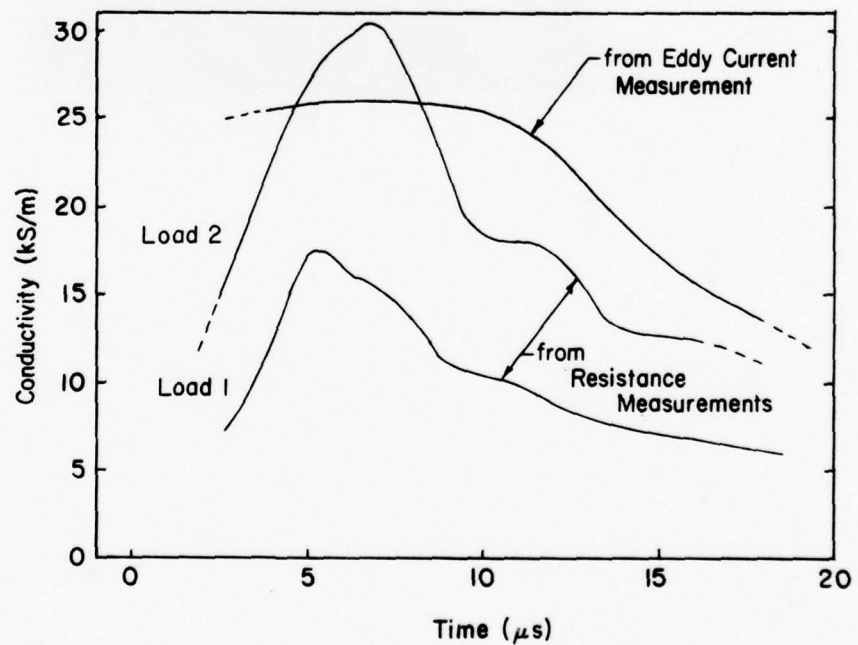


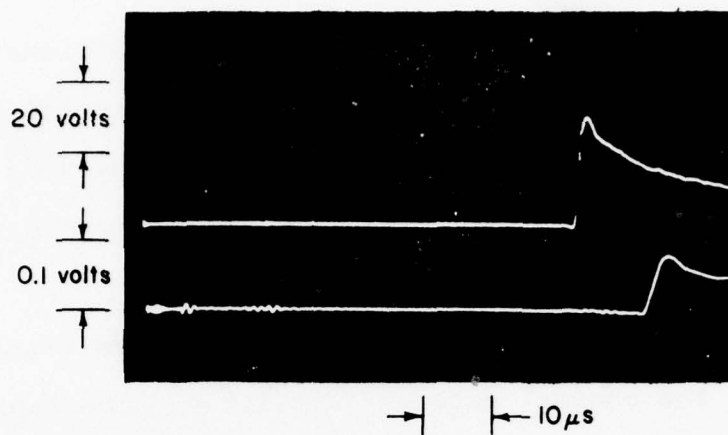
Figure 2.24 Plasma Conductivity History Obtained from Plasma Resistance Measurements and from Eddy Current Measurement on Shot 126-3

out in the lab by mocking up the shot conditions as closely as possible, and noise problems were eliminated by improving the RF shielding of the amplifier box. However, at the test site the noise problems recurred, and no meaningful data was obtained on the shot.

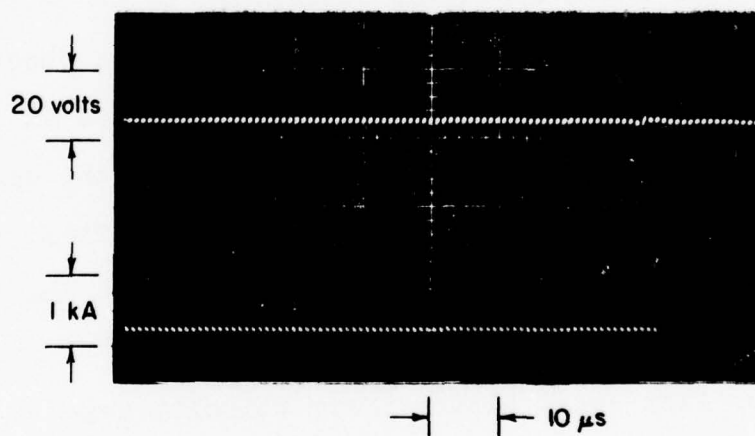
A malfunction of the triggering system resulted in the loss of the channel data on Shot 126-4. The scope records of the channel diagnostics on Shot 126-5 are shown in Figures 2.25 and 2.26. The records of Velocity Gage #2 and the Load Voltage were lost because of a scope trigger malfunction. From shock arrival times at the diagnostic stations in the channel the shock speed was determined to be 19.7 km/s, and the calculated initial flow speed behind the shock is 18.0 km/s. The record from Velocity Gage #1 gives an initial flow speed of 18.5 km/s which is 3% higher than the calculated value. The uncertainty in the effective B-field is about 5%, so the measured flow speed is correct within the limits of error of the velocity gage.

The flow speed history from Velocity Gage #1 is shown in Figure 2.27. The pulse duration was in excess of $26 \mu\text{s}$ with an average flow speed in that interval of 10 km/s.

The noise test on this shot was a simple one-turn pickup loop wrapped around the outside of the Lexan channel and located 25 mm downstream from V.G. #1. The signal (see Figure 2.25b) has a peak of about 0.6 volts and a duration of around $3 \mu\text{s}$. Subtracting this correction from the velocity

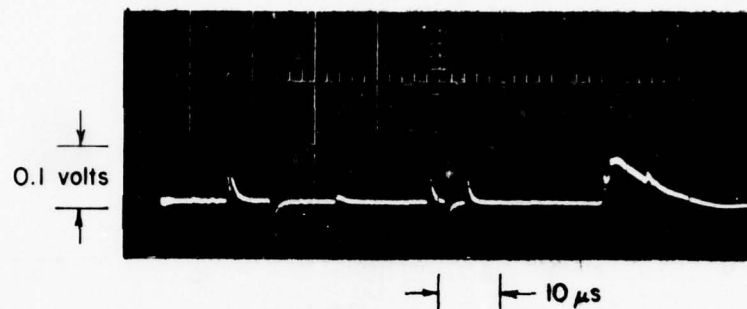


a. Velocity Gage No. 1 Output (Upper) and Conductivity Gage No. 2 Output (Lower) Versus Time

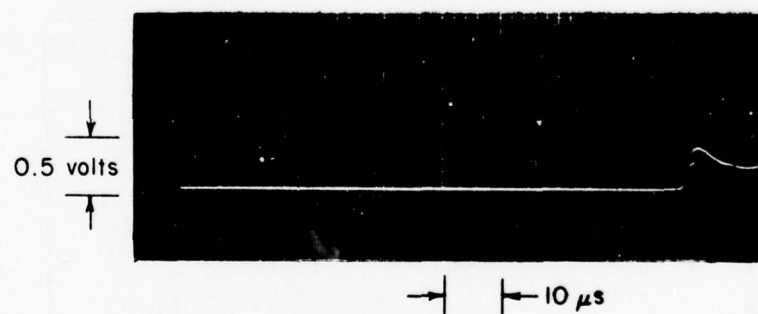


b. Noise Test Voltage (Upper) and Load Current (Lower) Versus Time

Figure 2.25 Channel Plasma Diagnostic Records for Shot 126-5



a. Conductivity Gage No. 1 Output Versus Time



b. Conductivity Gage No. 3 Output Versus Time

Figure 2.26 Conductivity Gage No. 1 and No. 3 Records for Shot 126-5

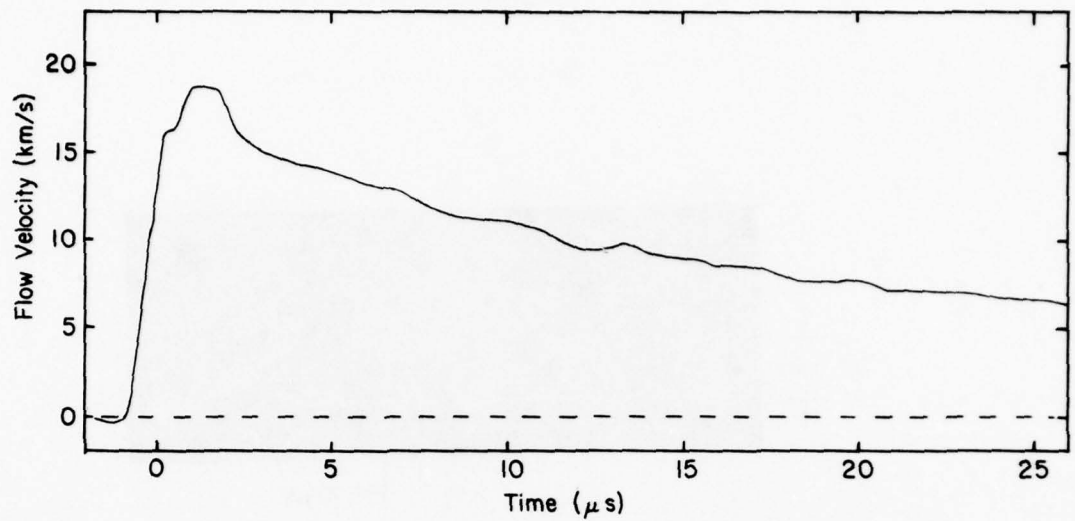


Figure 2.27 Velocity Gage Record of Plasma Flow Velocity History on Shot 126-5

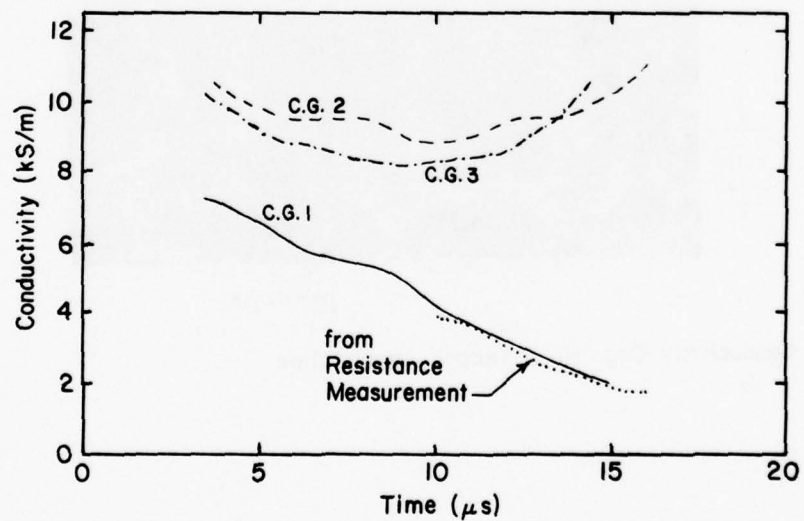


Figure 2.28 Plasma Conductivity Histories Obtained from Plasma Resistance Measurement and from Eddy Current Measurements on Shot 126-5

gage signal yields a value of 18.2 km/s for the initial flow speed. Using longer magnets has eliminated much of the noise by moving the source of the noise (axial B-field gradients at the ends of the magnets) at least several channel diameters away from the diagnostics.

Although the load voltage record was lost and the load current record is partly obscured, at least a partial plasma resistance history was obtained by using the measured amplitude (I) and slope (dI/dt) of the load current record. The corresponding effective conductivity is shown in Figure 2.28 together with the conductivity histories obtained from the three conductivity gages. Conductivity Gages #2 and #3 were at the same axial location, and the results agree within the accuracy of the measurements.

2.7 Experimental Observations

Summary of Experimental Performance Parameters

Explosive plasma sources are complex devices with time-varying output, and it is difficult to succinctly characterize their performance with specific parameter values. Nevertheless, for comparison and discussion purposes such characterization is useful.

Table 2.2 is a summary of experimental shock parameters. Since the channel shock velocity was found to be nearly constant, the tabulated values are accurate representations of plasma

TABLE 2.2

SUMMARY OF SHOCK PARAMETERS

Shot No.	Description	Nominal Piston Velocity (km/s)	Initial Channel Pressure (kPa)	Shock Velocity (km/s)	Shock Pressure (MPa)	Shock Energy Density (MJ/kg)
126-1	Asymmetric phased disc	16	1.3	13.1	2.37	149
126-2	Symmetric disc	8.5	1.3	23.6	7.54	467
126-3	Symmetric disc	8.5	4.0	31.8	40.8	835
126-5	Symmetric phased disc	12	4.0	19.7	15.7	324

TABLE 2.3

SUMMARY OF PLASMA PARAMETERS

Shot No.	Velocity (km/s)	Pulse Duration (μ s)	Conductivity (kS/m)	Total Specific Enthalpy (MJ/kg)	Nominal Mass (gram)	Comment
126-1	12.2	10	0.4	39	31	Gas seal inadequate
126-2	21.6	17	6.7	98	19	Aluminum flyer plate:
126-3	28.9	20	30	224	32	Steel flyer plates
126-5	18.0	26	10	65	28	Steel flyer plates

source output. Table 2.3 is a summary of measured plasma parameters, including velocity, pulse duration, conductivity, and enthalpy. In all cases there is a range of values of the parameter, and some judgement must be used to select a representative value. We have selected peak values for velocity and conductivity. Pulse duration was based on judgement, but usually corresponded to a fairly sharp drop in the oscilloscope record.

The tabulated value for total enthalpy represents the enthalpy of a fictitious stagnant reservoir of energized plasma which yields the measured shock velocity on expansion into the channel. It was selected as a reasonable method for characterizing plasma energy in a highly variable flow situation. The enthalpy is computed by a matching procedure: reservoir pressure is set by stagnating the nominal driver shock conditions, and reservoir enthalpy is varied until a match is achieved between computed shock velocity and measured shock velocity. The procedure is insensitive to the reservoir pressure assumption, and highly sensitive to the enthalpy. It is likely that the computed enthalpy is close to the actual value in the stagnation region, because the presumed expansion from stagnated gas is close to the real situation in a disc driver. We have not multiplied specific enthalpy by plasma mass to obtain total plasma enthalpy, because there is no way to determine how much of the plasma was energized and participated in the channel expansion.

The highest performance explosive plasma source in the test series was Shot 126-3, the unphased symmetric disc with steel flyer plates. Measured shock velocity was 31.8 km/s, and peak flow velocity corresponding to this value is 28.9 km/s. Peak conductivity was 30 kS/m, much higher than output from the other plasma sources. The actual data from this shot is shown in Figures 2.20 through 2.24.

A channel plasma pulse such as that observed on Shot 126-3 with a $20\mu\text{s}$ pulse of average flow velocity of 14 km/s and average effective conductivity of 10 kS/m (100 mho/cm) would give an 18 dB (factor of 7.8) magnetic field increase in a simple one-stage self-excited MHD circuit. If the average conductivity was 20 kS/m (200 mho/cm), it would be a 25 dB magnetic field increase in such a circuit. Although the effective conductivity data on Shot 126-3 is only provisional, the effective conductivity is probably in the range of 10-20 kS/m.

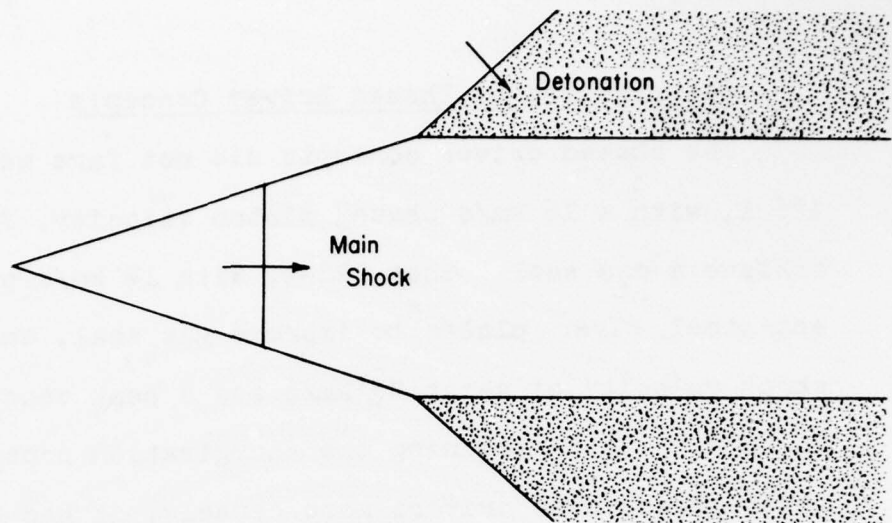
A 44 dB (factor of 150) increase in magnetic field is probably a reasonable criterion for a working MHD generator. Taking the results of Shot 126-3 and assuming 15 kS/m for the average effective conductivity and 14 km/s for the average flow velocity, to obtain a 44 dB B-field increase would require a pulse duration of $43\mu\text{s}$, a factor of two increase. Alternately if the pulse duration were $20\mu\text{s}$, an average flow velocity of 24 km/s would be required to obtain a 44 dB B-field increase. In other words the average flow velocity required is 70% greater than that obtained on the shot.

Observations on Phased Driver Concepts

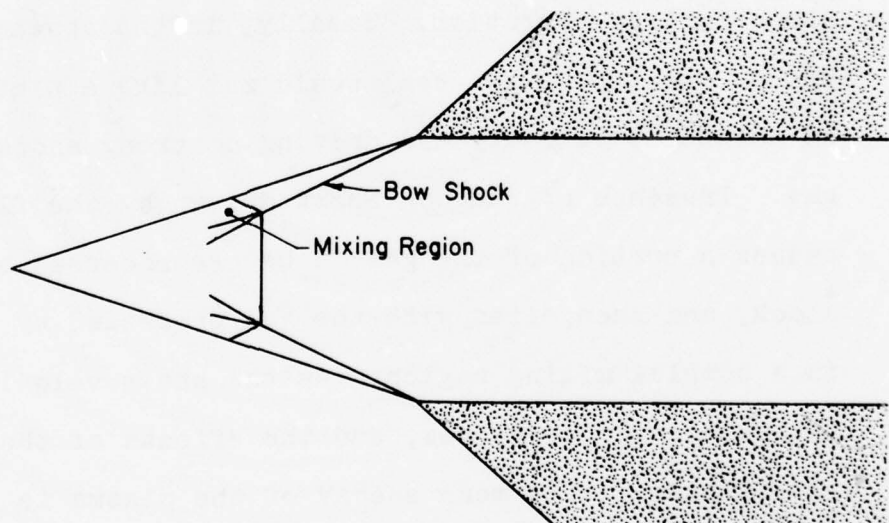
The phased driver concepts did not fare well. Shot 126-1, with a 16 km/s phased piston velocity, failed to achieve a gas seal. Shot 126-5, with 12 km/s phase velocity and steel flyer plates to improve gas seal, only produced a shock velocity of about 20 km/s and a peak conductivity of 10 kS/m. Upon examining the energization process for these phased disc drivers more closely, it was observed that the initial bow shock driven by the flyer plates plays an important role in the process.

Figure 2.29 shows the influence of the bow shock on phased driver operation. Ideally, in the absence of a bow shock, the impact gas seal would act like a piston traveling at the phase velocity and driving a strong shock into the gas. Presence of the bow shock driven by the flyer plates causes a portion of the gas to be preprocessed by a weaker shock, and then mixed with the gas processed by the main shock in a complex mixing region. As the phase velocity increases, the cone angle decreases, and the effects of the bow shock predominate. The mean energy of the plasma is therefore much less than would be expected if it were entirely processed by the high velocity main shock.

This observation does not mean that phased concepts are without merit, but rather that geometrical configurations must be found which minimize the effects of the weak subsidiary shock waves in the system.



a. Ideal Operation



b. Effects of Bow Shock

Figure 2.29 Influence of Bow Shock on Phased Driver Operation

Conductivity

One phenomenon generally observed is that the conductivities were relatively higher further downstream. On Shot 126-2 the conductivity gage, which was upstream of all other diagnostic stations, indicated that the conductivity was less than 0.44 kS/m, whereas Load #1 indicated a peak effective conductivity of more than 7 kS/m. On Shot 126-3 Load #1, which was the first diagnostic station, indicated a peak effective conductivity of about 17 kS/m, whereas both the conductivity gage and Load #2 indicated peak conductivities around 30 kS/m. On Shot 126-5 Conductivity Gage #1, the first diagnostic station, indicated a peak conductivity of less than 8 kS/m, whereas C.G. #2 and C.G. #3, which were both about 0.3 m downstream, indicated conductivities greater than 10 kS/m and which were increasing with time after 10 μ s.

The reason for this increase in conductivity is not presently known: it may be related to non-ideal plasma effects, boundary layer contaminations, or electrode corrosion. Since the plasma temperature and pressure are decreasing as the plasma expands downstream, most postulated mechanisms would indicate a decrease of conductivity rather than the observed increase.

3. THEORETICAL RESEARCH ON NON-IDEAL PLASMAS

3.1 Research Objectives

The primary objective of the theoretical effort is the determination of reliable values for the equilibrium thermodynamic properties and electrical conductivity of dense non-ideal plasmas. In view of the importance of the noble gases argon and xenon in the experimental effort, the calculational program has been directed towards the evaluation of thermodynamic properties for these two gases.

During the preceding ONR contract on dense plasmas (Reference 3.1), we carried out an extensive survey of the state of the art in thermodynamic property and conductivity calculations for dense plasmas. Based on our conclusions from that survey, we have decided to use the Debye-Huckel technique for equilibrium thermodynamic properties and Rogov's approach for electrical conductivity for our current calculational effort. In addition to generating calculated data on dense xenon and argon, a second important objective of the theoretical program is to delineate clearly the plasma regimes where these two approaches become invalid and where more accurate theories to account for quantum mechanical thermodynamic and transport effects are necessary.

During this contract period a considerable effort has been invested on the development of computer programs for carrying out the calculations. In this effort, we have been careful to ensure that the programs are computationally efficient and, equally importantly, that they are easily adaptable to the calculation of more complex plasma systems (a dense air plasma, for example).

The theory of ideal and non-ideal plasmas is outlined in the next section. Considerable emphasis is placed on ideal gas thermodynamics, and the Debye-Huckel correction for the non-ideal effects due to charged-particle interactions are introduced. The computational scheme is outlined in Section 3.3. Results of calculations of argon thermodynamic properties and conductivity are presented in Section 3.4, followed by those for xenon in Section 3.5.

3.2 Ideal and Non-Ideal Plasma Theory

3.2.1 Introduction

The purpose of this section is to outline the derivation of and to present final expressions for the equilibrium thermodynamic properties and the electrical conductivity of a monoatomic plasma. In the next subsection, we present the equilibrium thermodynamic theory based on the assumption that the plasma is a mixture of ideal gases. This treatment is followed, in Section 3.2.3, by a description of Debye-Huckel corrections for classical non-ideal effects resulting from charged particle interactions. Subsection 3.2.4 examines the plasma regimes where the Debye-Huckel approach is valid and discusses the appropriate length scales and the dimensionless ratios that are useful in characterizing the plasma. Methods useful for the calculation of electrical conductivity of dense non-ideal plasmas are then presented in the final subsection.

3.2.2 Equilibrium Thermodynamics of Ideal Gas Mixtures

The theory underlying ideal gas thermodynamic calculations has been presented in detail in many textbooks. However, there is a variety of notations and symbolic conventions. We will follow the approach and notation adopted by Zeldovich and Raizer (Ref. 3.2).

We start with the definition of the Helmholtz free energy Q in terms of the partition function F for a chemical

system occupying a volume V at a temperature T and containing N particles:

$$F = -kT \ln Q \quad (3.1)$$

Here,

$$Q = \sum \exp(-E_n/kT) \quad (3.2)$$

where the summation is carried out over all possible energy states (E_n 's) of the system.

The free energy is a thermodynamic potential with respect to V and T and once it has been determined, the entropy S , internal energy E and pressure P of the system can be determined from the following general thermodynamic relations:

$$S = -\left(\frac{\partial F}{\partial T}\right)_{V,N} \quad (3.3)$$

$$E = F + TS = -T^2 \frac{\partial}{\partial T} \left(\frac{F}{T}\right)_{V,N} \quad (3.4)$$

$$P = -\left(\frac{\partial F}{\partial V}\right)_{T,N} \quad (3.5)$$

The expressions (3.1) through (3.5) are very general in that they are independent of any assumptions regarding the nature of the interparticle forces. We now introduce the ideal gas assumption, i.e.: that the particles are non-interacting. In that case, the system partition function defined in Equation (3.2) may be factored into a product of co-factors, each corresponding to the particles of one kind

$$Q = \frac{Z_A^{N_A}}{N_A!} \frac{Z_B^{N_B}}{N_B!} \dots \quad (3.6)$$

Here, Z_A, Z_B etc. are the partition functions of each type for one molecule and can be expressed by equations of a form similar to Equation (3.2) for the system partition function:

$$Z = \sum_k \exp(-E_k/kT) \quad (3.7)$$

In Equation (3.7), E_k is the energy of a particle in state k and the summation is carried out over all possible states of one molecule.

Using Equations (3.1) and (3.6) together with Stirling's formula $[N! \approx (N/e)^N]$ we can write the free energy of an ideal gas mixture in the form

$$F_{id} = -N_A kT \ln\left(\frac{Z_A e}{N_A}\right) - N_B kT \ln\left(\frac{Z_B e}{N_B}\right) - \dots \quad (3.8)$$

From here on, we restrict our attention to a plasma resulting from the ionization of a single monoatomic species such as argon or xenon. In the case of a pure argon plasma, for example, the plasma would consist of electrons, argon atoms, and argon ions. If we adopt the subscript m to denote an ion with charge equal to m and consider atoms as a special case of an m -ion with $m=0$ we can re-express the free energy of the system in the form

$$F_{10} = - \sum_m N_m kT \ln \left(\frac{Z_m e}{N_m} \right) - N_e kT \ln \left(\frac{Z_e e}{N_e} \right) \quad (3.9)$$

In Equation (3.9), Z_m and Z_e are the partition functions for an m -ion and an electron, respectively. Since we are considering monoatomic species, there are no rotational and vibrational contributions to Z_m and we may factor out the translational and electronic contributions to Z_m as

$$Z_m = Z_m^{\text{tr}} Z_m^{\text{el}} \quad (3.10)$$

The electron partition function consists of the translational contribution Z_e^{tr} and the degeneracy factor of two resulting from the two possible spin states of an electron, i.e.

$$Z_e = 2 Z_e^{\text{tr}} \quad (3.11)$$

In general the translational contribution can be written (with i set to m for an m -ion and e for an electron) as:

$$\begin{aligned} Z_i^{\text{tr}} &= (2\pi m_i kT/h^2)^{3/2} V \\ &= f_i (kT)^{3/2} V \end{aligned} \quad (3.12)$$

where m_i is the mass of an i -th particle and where we have introduced the notation

$$f_i = (2\pi m_i / h^2)^{3/2}, \quad i = m \text{ or } e \quad (3.13)$$

Before expressing the electronic contribution (Z_m^{el}) to the total partition function it is useful to describe the convention we have chosen to represent the ionization potentials and the electronic energy levels of the various m -ions. Successive ionization potentials are described by I_m i.e., I_1 is the energy required to remove the first electron from a neutral atom, etc. (note that $I_0 = 0$). It is also convenient to introduce the notation E_0^m to represent the cumulative ionization potential of an m -ion i.e.: the energy required to remove m electrons from an atom. Thus we have

$$E_0^m = I_1 + I_2 + \cdots + I_m = \sum_{p=1}^m I_p, \quad (I_0 = 0) \quad (3.14)$$

and, conversely,

$$I_m = E_0^m - E_0^{m-1} \quad (3.15)$$

This convention is graphically illustrated in Figure 3.1a.

Figure 3.1b shows the convention used for denoting electronic energy levels. Consider the k th electronic energy level of an m -ion. We use E_k^m to denote the energy of this level with respect to the ground electronic state of the neutral atom and w_k^m to denote the energy difference with respect to the ground electronic state of the m -ion itself. Clearly then

$$E_k^m = E_0^m + w_k^m$$

and the electronic contribution to the partition function of the m -ion can be written (using g_k^m to denote the degeneracy of the k level of the m -ion)

$$\begin{aligned} Z_m^{el} &= \sum_k g_k^m \exp(-E_k^m/kT) \\ &= \exp(-E_0^m/kT) \sum_k g_k^m \exp(-w_k^m/kT) \end{aligned} \quad (3.16)$$

If we introduce the notation

$$u_m(T) = \sum_k g_k^m \exp(-w_k^m/kT) \quad (3.17)$$

then

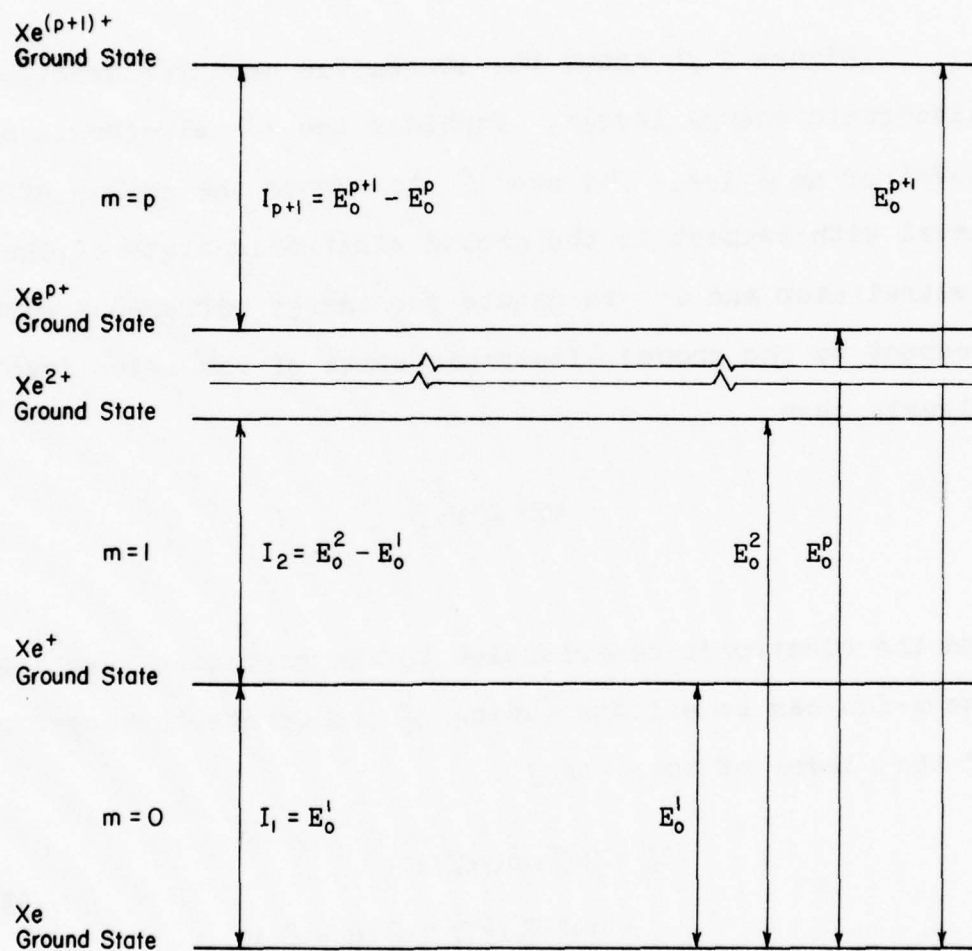


Figure 3.1a Convention Used in Denoting Ionization Potential (I_m) and Cumulative Ionization Potential (E_o^m).

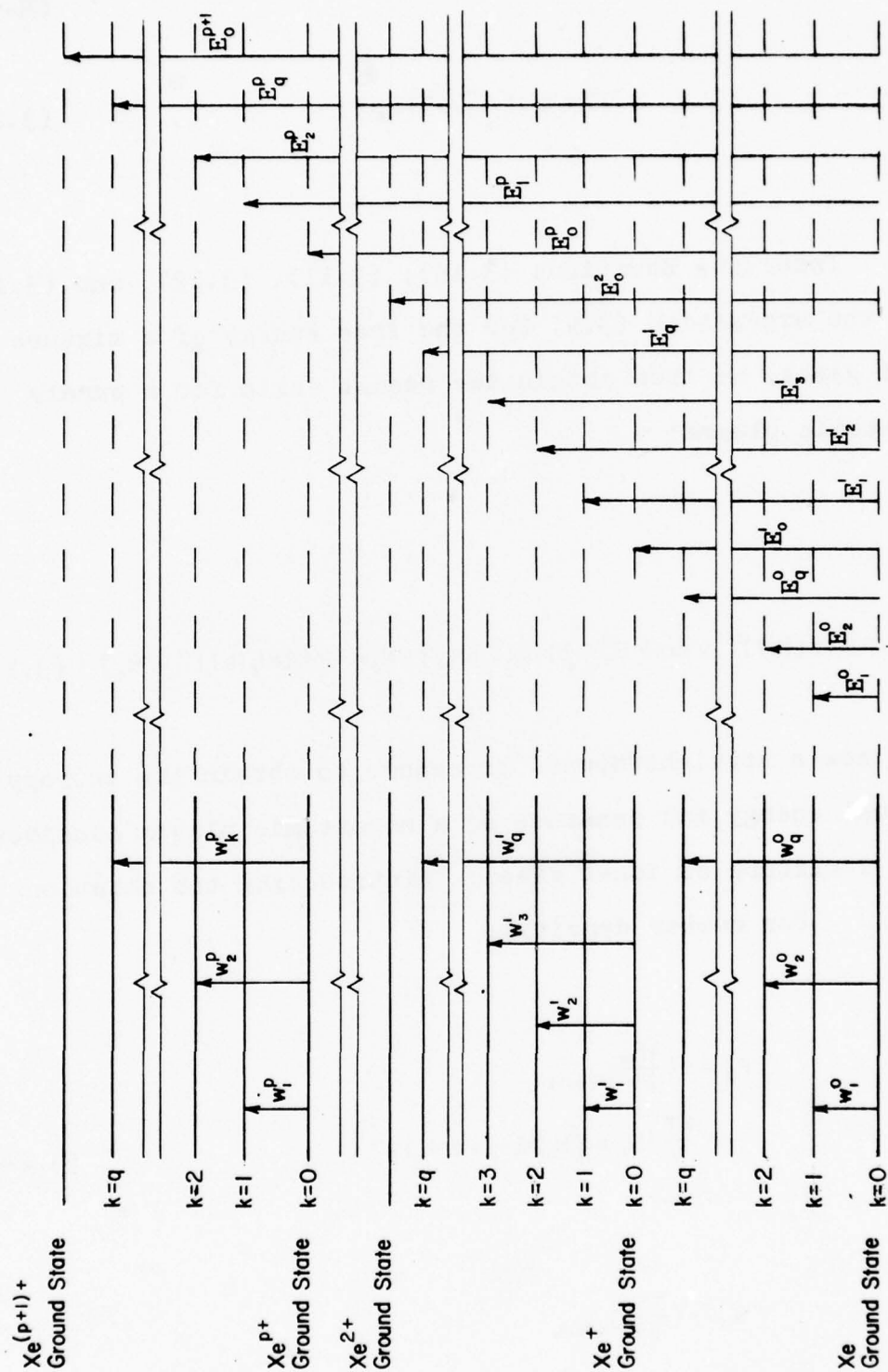


Figure 3.1 b Convention Used in Denoting Electronic Energy Level (E_k^m) of m -ion with Respect to Ground State of Neutral Atom and Electronic Energy Level of m -ion with Respect to Ground State of m -ion (w_k^m).

$$Z_m^{\text{el}} = \exp(-E_0^m/kT) u_m(T) \quad (3.18)$$

Inserting Equations (3.10), (3.11), (3.12), and (3.18) into the expression (3.9) for the free energy of a mixture of ideal gases, we then obtain the result valid for a purely monoatomic plasma:

$$F_{10} = -\sum_m N_m kT \ln [e f_m(kT)^{3/2} V \exp(-E_0^m/kT) u_m(T)/N_m] - N_e kT \ln [2e f_e(kT)^{3/2} V/N_e] \quad (3.19)$$

It is now a straightforward procedure to obtain the entropy, internal energy and pressure of a monoatomic plasma considered to be a mixture of ideal gases: (introducing the notation $n_i = N_i/V$ for number density):

$$\begin{aligned} P_{10} &= -\left(\frac{\partial F_{10}}{\partial V}\right)_{T, N_m, N_e} \\ &= \frac{kT}{V} (N_e + \sum_m N_m) = (n_e + \sum n_m) kT \end{aligned} \quad (3.20)$$

$$\begin{aligned} S_{10} &= -\left(\frac{\partial F_{10}}{\partial T}\right)_{V, N_m, N_e} \\ &= \sum N_m k \ln [e^{5/2} f_m(kT)^{3/2} u_m(T) V/N_m] \\ &\quad + N_e k \ln [2e^{5/2} f_e(kT)^{3/2} V/N_e] + \frac{1}{T} \sum N_m V_m / u_m(T) \end{aligned} \quad (3.21)$$

where

$$V_m(T) = \sum_k g_k^m w_k^m \exp(-w_k^m/kT) \quad (3.22)$$

In Equation (3.22), g_k^m is the degeneracy of the k th electronic energy level of the m -ion.

It is more convenient to work with the dimensionless specific entropy s_{10}/R which is related to the total entropy of the system (note: system mass $M = m_0 \sum N_m = m_0 N$ where m_0 is the mass of a neutral atom and N is the total number of nuclei present in the system. Both M and N remain constant for an isolated system) as follows:

$$\begin{aligned} \frac{s_{10}}{R} \equiv \frac{S_{10}}{MR} = & \frac{5}{2}(1 + \alpha_e) + \sum_m \alpha_m \ln \frac{u_m(T)}{N_m} + \frac{1}{kT} \sum_m \alpha_m \frac{V_m}{u_m} \\ & + \ln[f_m(kT)^{3/2}] + \alpha_e \ln[2 f_e(kT)^{3/2}/n_e] \end{aligned} \quad (3.23)$$

In Equation (3.23) we have introduced α_m and α_e to represent the degrees of ionization of m -ions and electrons respectively. They are defined by

$$\alpha_m = \frac{N_m}{\sum_m N_m} = \frac{N_m}{N} = \frac{n_m}{n} \quad (3.24)$$

and

$$\alpha_e = \frac{N_e}{\sum_m N_m} = \frac{N_e}{N} = \frac{n_e}{n} \quad (3.25)$$

We point out that the principles of conservation of charge and mass imply

$$\sum_m \alpha_m = \sum_m N_m / N \equiv 1 \quad (3.26)$$

and

$$\sum_m m \alpha_m = \sum_m m N_m / N = N_e / N = \alpha_e \quad (3.27)$$

Finally, the internal energy is easily derived by substitution of Equation (3.9) into Equation (3.4):

$$E_{io} = \frac{3}{2} kT(N_e + \sum_m N_m) + \sum_m N_m \frac{V_m}{u_m} + \sum_m N_m E_o^m \quad (3.28)$$

or, the specific internal energy e_{io} is given by

$$e_{io} = \frac{E}{M} = \frac{E}{m_o N} = \frac{1}{m_o} \left[\frac{3}{2} kT(1 + \alpha_e) + \sum_m \alpha_m \frac{V_m}{u_m} + \sum_m \alpha_m E_o^m \right] \quad (3.29)$$

It is clear that the right hand side of Equation (3.29) comprises the contributions to the total specific internal energy from three components: translation, ionization and electronic excitation:

$$e_{io} = e_{tr} + e_{ioniz} + e_{el exc} \quad (3.30)$$

where

$$e_{tr} = \frac{3}{2} kT(1 + \alpha_e) / m_0 \quad (3.31)$$

$$e_{el exc} = \frac{1}{m_0} \sum \alpha_m \frac{V_m}{U_m} \quad (3.32)$$

and

$$e_{ioniz} = \frac{1}{m_0} \sum \alpha_m E_0^m \quad (3.33)$$

It is necessary to determine the equilibrium concentrations of the various constituent species (ions, atoms and electrons) of the plasma. The standard procedure is to consider the ionization reaction

$$A_m \rightleftharpoons A_{m+1} + e, \quad m = 0, 1, 2, \dots \quad (3.34)$$

and apply the principle that, under conditions of thermodynamic equilibrium, the free energy F is a minimum with respect to the number of particles. This procedure leads to the so-called Saha equation:

$$\frac{n_{m+1} n_e}{n_m} = 2 f_e (kT)^{3/2} \frac{u_{m+1}(T)}{u_m(T)} \exp[-(E_0^{m+1} - E_0^m)/kT] \quad (3.35)$$

It is useful to define the partial pressures

$$P_i = n_i kT \quad (i = m \text{ or } e) \quad (3.36)$$

from which we can re-express the Saha equation in a form that is more convenient for computational purposes:

$$\frac{P_{m+1}}{P_m} = \frac{2f_a}{P_0} (kT)^{3/2} \frac{u_{m+1}(T)}{u_m(T)} \exp[-(E_0^{m+1} - E_0^m)/kT] \quad (3.37)$$

Questions regarding the validity of the ideal gas assumption will be taken up in Subsection 3.2.4 after we have outlined the Debye-Huckel procedure to account for non-ideal effects arising from interparticle coulomb interactions. The discussion of efficient computational schemes based on the ideal gas approximation are relegated to Section 3.3.

3.2.3 The Debye-Huckel Correction to Ideal Gas Theory

The Debye-Huckel theory (References 3.1 to 3.4) has been widely used in computing the equilibrium thermodynamic properties of weakly non-ideal plasmas. The method is based on an approximate evaluation of the screening effect of the surrounding charges on the potential of a given ion using classical electrostatics and Boltzmann statistics.

The application of this theory (see References 3.1 to 3.4 for detailed derivations) leads to the following expression for the correction term ΔE to the internal energy of the system:

$$\Delta E^{DH} = -e^3 (\pi/kTV)^{1/2} (N_0 + \lambda \sum_m m^2 N_m)^{3/2} \quad (3.38)$$

In Equation (3.38), λ is an arbitrary parameter which may take any value between 0 and 1 and which determines the extent of ionic participation in the coulombic screening process.

The first step in deriving the Debye-Huckel expressions for pressure, entropy, and species number densities is to derive the DH (Debye-Huckel) correction to the free energy of the system. This is easily shown to be (m is the charge of the m -ion)

$$\Delta F^{DH} = -\frac{2}{3} e^3 (\pi/kTV)^{1/2} (N_0 + \lambda \sum_m m^2 N_m)^{3/2} = \frac{2}{3} \Delta E^{DH} \quad (3.39)$$

and then we have

$$F^{DH} = F^{ID} + \Delta F^{DH} \quad (3.40)$$

With the aid of the general thermodynamic relation 3.3 through 3.5, we can obtain:

$$P^{DH} = P^{ID} + \Delta P^{DH}$$

where

$$\Delta P^{DH} = -\frac{1}{3} e^3 (\pi/kT)^{1/2} (n_e + \lambda \sum_m m^2 n_m)^{3/2} \quad (3.41)$$

or

$$\Delta P^{DH} = -e^2 (n_e + \lambda \sum_m m^2 n_m) / 6D_\lambda \quad (3.42)$$

where the generalized Debye length D_λ is defined

$$D_\lambda = [kT/4\pi e^2 (n_e + \lambda \sum_m m^2 n_m)]^{1/2} \quad (3.43)$$

The entropy correction can be shown to be

$$\Delta s^{DH}/R = -[24\pi D_\lambda^3 n]^{-1} \quad (3.44)$$

The Saha Equation for a Debye-Huckel plasma can be shown to be

$$n_{m+1} n_e / n_m = 2f_e (kT)^{3/2} (u_{m+1}/u_m) \exp[-(E_0^{m+1} - E_0^m + \Delta I_{m+1})/kT] \quad (3.45)$$

where f_e has been defined by Equation (3.13) and the Debye-Huckel correction to the ionization potential, ΔI_m is defined by

$$\Delta I_m = -e^2 (2\lambda m - \lambda + 1) / 2D_\lambda \quad (3.46)$$

If we define DH-corrected cumulative ionization potentials

$$E_o^{m,DH} = E_o^m - e^2 (\lambda m^2 + m) / 2D_\lambda, \quad (3.47)$$

we can rewrite the Saha equation (using partial pressures in place of number densities)

$$P_{m+1}^{DH} / P_m^{DH} = [2f_e (kT)^{3/2} / P_e] (u_{m+1} / u_m) \exp[-(E_o^{m+1,DH} - E_o^{m,DH}) / kT] \quad (3.48)$$

The Debye-Huckel thermodynamic expressions are thus qualitatively similar to those for the ideal gas case and hence the computational procedure is essentially the same.

3.2.4 Validity of the Ideal Gas Approximations and the Debye-Huckel Theory

The ideal gas approach is based on the presumption that particle number densities are low enough and temperatures high enough that the average interparticle energies are much smaller than the random (thermal) kinetic energy. For a strongly

ionized plasma, $\bar{Z}^2 e^2 / n_c^{-1/3}$ is a measure of the average electrostatic interaction energy of the charged particles and thus the ideal gas assumption implies that

$$\text{INTPAR} \equiv \bar{Z}^2 e^2 n_c^{1/3} / kT \ll 1 \quad (3.49)$$

where INTPAR denotes the so-called interaction parameter of the plasma. In Equation (3.49), \bar{Z}^2 is the mean square charge

$$\bar{Z}^2 = (n_e + \sum_m m^2 n_m) / n_c \quad (3.50)$$

where n_c is the total charged particle number density, i.e.:

$$n_c = n_e + \sum_{m=1}^{\infty} n_m \quad (3.51)$$

In Reference 3.1, we reported estimates of the interaction parameter at conditions typical of the dense plasmas produced in explosive-driven shock tubes. Calculations based on the ideal gas assumption at pressure of 1 GPa and at 3.6×10^{11} J/kg specific internal energy gave an INTPAR value of 0.57. This is clearly outside the range of applicability of the ideal gas assumption.

The conditions under which the Debye-Huckel approach is valid has been discussed by several authors (References 3.3

and 3.4). A fairly restrictive condition that is often applied is that the Debye sphere contain a large number of charged particles. However, Reference 3.3 has presented a less restrictive condition (which has been derived on the basis of a classical statistical mechanical study of weak electrolyte solutions):

$$n_c = n_e + \sum_{m=1}^{\infty} n_m \geq (8\pi D)^{-1} \quad (3.52)$$

Physically Equation (3.52) can be interpreted as requiring at least one-sixth of a charged particle in the Debye sphere in order for the Debye-Huckel theory to be valid.

It is more convenient to express the condition (3.52) in terms of the interaction parameter:

$$\text{INTPAR} \leq \pi^{-2/3} = 0.47 \quad (3.53)$$

Both the ideal gas approximation and the Debye-Huckel correction for coulombic interactions are based on a completely classical treatment of the problem. However, under conditions of sufficiently high density, it is essential to account for quantum mechanical effects. These quantum effects and the dimensionless parameters that are helpful in indicating their relative importance have been discussed in detail in Reference 3.1.

3.2.5 Electrical Conductivity

In the context of the preceding ONR contract, we had carried out a thorough literature survey of techniques for calculating the electrical conductivity of dense plasmas. As a result of that survey, we concluded that there are two methods that can be applied to the calculation of xenon and argon conductivities.

The first technique is the well-established Spitzer-Harm method (Reference 3.5) which provides a simple expression valid under the condition that:

$$\ln \Lambda = \ln[(3/2 \pi)^{1/2} (\text{INTPAR})^{3/2}] \gg 1 \quad (3.54)$$

Using 0.6 as a typical value of INTPAR under conditions of interest to us, we obtain $\ln \Lambda = 0.6$. Hence the Spitzer-Harm technique is not expected to be very useful for our purposes.

A better method for calculation of electrical conductivity at plasma conditions of interest to us is that due to Rogov (Reference 3.6). Unlike the Spitzer-Harm approach which is based on completely classical mechanical concepts, Rogov's theory accounts for quantum mechanical short-range collisional effects which are known to have an important contribution to the transport integrals for dense

plasmas. Rogov uses the Born Approximation and a Debye-shielded potential within the framework of a fourth-order Chapman-Enskog approach and, in the high temperature asymptotic limit, his result for electrical conductivity takes the simple form

$$\sigma_R = 9.697 T^{3/2} \beta(Z) / Z \ln \Lambda_R \quad (\text{kS}\cdot\text{m}^{-1} \text{ if } T \text{ in eV}) \quad (3.55)$$

In Equation 3.55, Z is the average ionic charge ($Z = n_e^{-1} \sum m^2 n_m$), $\beta(Z)$ is a tabulated function of Z and Λ_R is the ratio of the Debye-length (with both ionic and electron shielding, i.e.: $\lambda=1$) and the electron DeBroglie wavelength:

$$\Lambda_R = 2D / \lambda_e \quad (3.56)$$

where

$$\lambda_e = h / (2m_e kT)^{1/2} \quad (3.57)$$

The Spitzer-Harm expression is qualitatively similar to Rogov's result:

$$\sigma_{SH} = 32.90 T^{3/2} \alpha(Z) / Z \ln \Lambda \quad (\text{kS}\cdot\text{m}^{-1} \text{ if } T \text{ in eV}) \quad (3.58)$$

where Λ is the plasma parameter of Equation (3.54) and is defined by

$$\Lambda = D_1 / \bar{b}_0 = (3/2 \pi^{1/2}) (T / Z^2 e^2)^{3/2} n_c^{-1/2} = (3/2 \pi^{1/2}) \text{INTPAR}^{-3/2} \quad (3.59)$$

\bar{b}_0 is the average impact parameter for 90° scattering ($\bar{b}_0 = \bar{Z}^2 e^2 / 3 kT$). We note that it is principally in the definition of an effective plasma parameter (Λ or Λ_R) that the two theories differ.

3.3 Computational Methods

3.3.1 Introduction

In the final report for the preceding contract (Reference 3.1), we had presented a few benchmark calculations of equilibrium thermodynamic properties and conductivity for argon and xenon. During the current contract, we devoted a significant amount of effort towards the development of a number of computer programs which enable rapid calculation of these quantities using either the ideal gas approximation or two variants of the Debye-Huckel approach.

Our objective in developing these programs was to have at hand a means for carrying out calculations over a very wide range of pressures (0.1 MPa to 10 GPa) and of specific internal energies (2 MJ/kg to 2.5 GJ/kg) and for

presenting these results in the form of Mollier charts. In this section we will discuss the purely computational aspects of our effort and take up presentation and discussion of the results for xenon and argon in the two following sections.

3.3.2 Recasting the Basic Equations in a Form Convenient for Computation

We will now recast the equations presented in Section 3.2 for the three following methods of calculations:

- (1) Ideal Gas Approximation (ID)
- (2) Debye-Hückel Approximation with full ionic contribution to shielding,
i.e.: $\lambda = 1$ (DH1)
- (3) Debye-Huckel Approximation without any ionic participation in shielding,
i.e.: $\lambda = 0$. (DHO)

The first computational task is to solve the set of Saha equations subject to the charge and mass conservation constraints. The input data needed are the electronic energy levels and the ionization potentials of the m -ions: $m = 0, 1, 2, 3, \dots, m^*$. We will illustrate the computational scheme using the ideal gas case as our example. The differences in handling the DHO and DH1 schemes will then be outlined.

Ideal Gas Approximation:

The plasma consists of m^*+1 types of heavy particles (ions and atoms) and electrons, i.e. (m^*+2) "species" in all. We can rewrite the Saha equations (3.37) in the form:

$$P_m/P_0 = B^m (u_m/u_0) \exp(-E_0^m/kT), \quad (m=1, 2, \dots, m^*) \quad (3.60)$$

where the dimensionless quantity B is defined by

$$B = 2f_e (kT)^{5/2} / P_e \quad (3.61)$$

We also recall [Equation (3.17)] the partition function

$$u_m(T) = \sum_{k=0}^{\infty} g_k^m \exp(-w_k^m/kT) \quad (3.62)$$

where $w_k^m = E_k^m - E_0^m$ is the energy of the k th electronic level of the m -ion and the sum in (3.62) is over all electronic energy levels.

We digress for a moment to point out that in principle, for an isolated atom or ion, the sum in Equation (3.62) is divergent. The various methods for handling this problem have been discussed in Reference 3.1. We merely point out that we simply use all known electronic energy levels in computing the partition function sum. This divergence is not a problem in the Debye-Huckel approach because of the lowering of the

ionization potential which results when inter-particle interactions are accounted for. We also point out that because the lowering of the ionization potential may depend on thermodynamic variables other than T the partition function in such a computation may be dependent on more than just the temperature.

Using the definition of partial pressure, Equation (3.36), the charge and mass conservation conditions represented by Equations (3.26) and (3.27) may be rewritten

$$\sum m P_m = P \quad (3.63)$$

$$\sum P_m = nkT \quad (n = \sum_{m=0}^{\infty} n_m) \quad (3.64)$$

From Equation (3.20) we also have

$$P = (\sum n_m + n_e) kT = \sum P_m + P_e \quad (3.65)$$

The Saha Equations together with the conditions represented by Equations (3.63) through (3.65) are a determinate system provided any two thermodynamic variables are taken as initial values. Clearly P_e and T are the most convenient choice for the independent variables. We now outline the computational steps starting with given values of P_e and T :

1. Given T , compute partition function $u_m(T)$ and the function $v_m(T)$ in Equation (3.22).
2. Calculate the ratios P_m/P_0 using Equation (3.60), for $m=1, 2, \dots, m^*$.
3. Compute $A = \sum_{m=0}^{m^*} m P_m/P_0$
4. Compute $P_0 = P_e/A$
5. Calculate $P_m = (P_m/P_0) P_0$, $m=1, 2, \dots, m^*$ and hence P from Equation (3.65).
6. Calculate $n_i = P_i/kT$, $i=e$ or $m (=0, 1, \dots, m^*)$ and then calculate $n = \sum n_m$
7. Calculate mass density $\rho = nm_0$ where m_0 is the mass of an atom.
8. Calculate the ionization fractions $\alpha_i = n_i/n$, $i=e$ or $m (=0, 1, \dots, m^*)$
9. Compute specific internal energies using Equation (3.29).
10. Compute specific enthalpy, $h = e + p/\rho$
11. Calculate the effective isentropic exponent, $\gamma = h/e$
12. Calculate specific dimensionless entropy s/R using Equation (3.23).
13. Calculate the speed of sound, $a = (\gamma P/\rho)^{1/2}$
14. Calculate electrical conductivity using the Spitzer-Harm expression, Equation (3.58), or Rogov's asymptotic expression, Equation (3.55).

Debye-Huckel Theory with No Ion Participation in Shielding

The major difference here is the reduction in ioniza-

AD-A063 386

ARTEC ASSOCIATES INC HAYWARD CALIF
RESEARCH ON NON-IDEAL PLASMAS.(U)
JUL 78 D W BAUM, S P GILL, W L SHIMMIN

F/G 20/9

UNCLASSIFIED

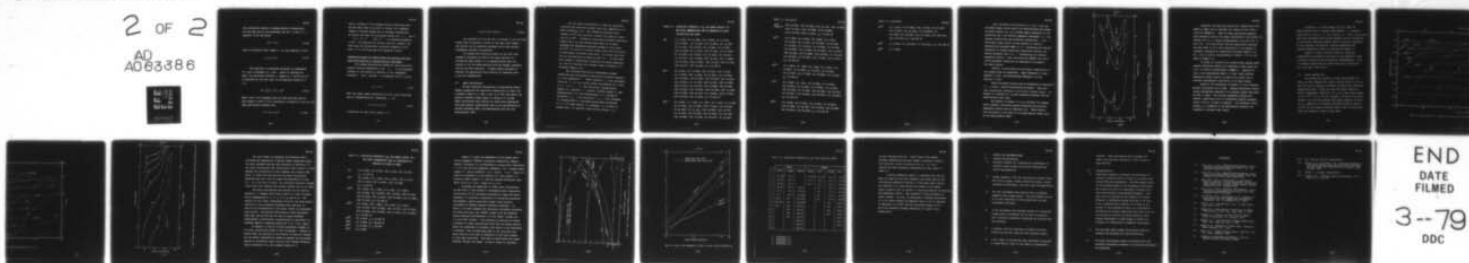
FR-126

N00014-77-C-0463

NL

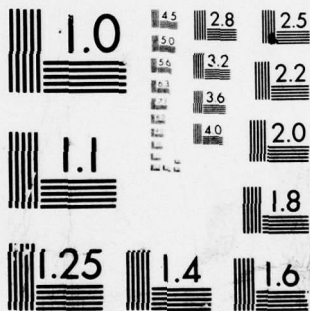
2 OF 2

AD
A063386



END
DATE
FILMED

3--79
DDC



MICROCOPY RESOLUTION TEST CHART
NATIONAL BUREAU OF STANDARDS-1963-A

tion potentials induced by charged-particle interactions.

For the case with no ion shielding, use set $\lambda = 0$ and $D_\lambda = D_0$ in Equation (3.46) and obtain

$$\Delta I_m^{\text{DHO}} = -e^2/2 D_0 \quad (3.66)$$

where the modified Debye length D_0 is [see Equation (3.43)]

$$D_0 = (kT/4\pi e^2 n_0) \quad (3.67)$$

The reduction in ionization potential is independent of m and is dependent on P_e and T . Hence in carrying out step 1 the partition functions u_m depend on P_e as well as on T . In carrying out the next step, we use modified values of E_0^m i.e.:

$$E_0^{m,\text{DHO}} = \sum_{p=1}^m I_p^{\text{DHO}}, \quad I_p^{\text{DHO}} = I_p + \Delta I_p^{\text{DHO}} \quad (3.68)$$

Steps 3 and 4 are unchanged from the ideal gas case and the only change in step 5 is the replacement of Equation (3.65) for the ideal gas mixture pressure with

$$P^{\text{DHO}} = \sum P_m + P_e + \Delta P^{\text{DHO}} \quad (3.69)$$

Steps 6 through 11 are unchanged from the ideal gas case. We note that there is no need to account for a separate change in internal energy due to coulombic interactions as long as one uses the appropriate values for u_m , v_m and E_o^m (i.e. u_m^{DHO} , v_m^{DHO} and $E_o^{m,DHO}$) in evaluating Equation (3.29). In computing the entropy (step 12), however, one must apply the Debye-Huckel correction [Equation (3.44) with $\lambda=0$] to the ideal gas form [Equation (3.23)].

Computation Scheme for Debye-Huckel Calculations with Full Ionic Participation in Charged-Particle Shielding:

The primary modification needed for this calculation results from the dependence of the ΔI_m on one dependent variable of the problem in addition to the independent variables T and P_o . Setting $\lambda=1$ in Equation (3.46) we have

$$\Delta I_m^{DHI} = -me^2/D_1 \quad (3.70)$$

where the Debye length appropriate for full ionic participation in (charged-particle) shielding, D_1 is:

$$D_1 = [kT/4\pi e^2 n_e (1+Z)]^{1/2} \quad (3.71)$$

Z represents the mean ionic charge, i.e.,

$$Z = \sum m^+ n_m / \sum m n_m = n_e^{-1} \sum m^+ n_m \quad (3.71a)$$

The procedure for the DH1 case is similar to the DHO case, except that one guesses a value for the mean ionic charge Z and carries out an iteration procedure until some suitable convergence criteria is satisfied.

In closing this section we point out the fact that instead of choosing the atom as the pivot particle in solving the Saha system, it is computationally more convenient to use the heavy particle with the largest concentration as the pivot particle. A simple search procedure to identify the appropriate pivot particle is therefore used in all our computations.

3.4 Argon Calculations

We have completed calculations of equilibrium thermodynamic properties and electrical conductivity of argon over a pressure range of 0.1 MPa (1 bar) to 10 GPa (100 kbars) and specific internal energy range of 2 MJ/kg to 2.5 GJ/Kg. These calculations were carried out using three approaches: ideal gas mixture, Debye-Huckel with no ion participation in Coulomb shielding (DHO), and Debye-Huckel with full ion participation (DH1).

For the argon calculations, we used the ionization potential and electronic energy level data compiled by C.E. Moore (Reference 3.8). Her ionization potential data extends to Ar^{8+} and electronic energy level data for argon ions up to Ar^{7+} . Instead of using each individual electronic energy level, we used energy groups about an eV apart obtained from degeneracy-weighted averages of the levels. For Ar^{8+} , for which no electron energy level data were given, we used simply the ground state data. The actual data used for our calculations are shown in Table 3.1. In this table each integer in parenthesis represents the group degeneracy (g_k^m) and the floating point decimal number following it is the group energy in eV.

The following equilibrium thermodynamic plasma properties were calculated as functions of electron pressure (p_e) and temperature T : number densities (n_i) and ionization fractions (α_i) of the various plasma constituents [i.e. atom ($m=0$), ions ($m=1, \dots, m^*$) and electrons]; average square charge (\bar{Z}^2); pressure (P); specific internal energy (e) and contributions to it from translational (e_{tr}), electronic excitation ($e_{el\ exc}$) and ionization (e_{ioniz}); the flowspeed (u) corresponding to e assuming strong shock processing [i.e. $u=(2e)^{1/2}$]; mass density (ρ); enthalpy (h); enthalpy to energy ratio (γ); specific dimensionless entropy (s/R).

Table 3.1 IONIZATION POTENTIALS (I_m) AND ENERGY GROUPS (eV)
AND GROUP DEGENERACIES USED IN EQUATION OF STATE
CALCULATIONS FOR ARGON

Ar^0 : (1) 0.0000, (5) 11.5480, (3) 11.6230, (1) 11.7230,
(3) 11.8280, (3) 12.9067, (12) 13.0800, (8) 13.1606,
(1) 13.2727, (8) 13.2933, (4) 13.3900, (4) 13.7966,
(16) 13.8549, (8) 13.9975, (20) 14.0781, (16) 14.2269,
(8) 14.2579, (3) 14.4637, (12) 14.5009, (8) 14.5269,
(1) 14.5756, (16) 14.6955, (36) 14.7910, (56) 14.9088,
(20) 14.9645, (32) 15.0947, (36) 15.1505, (56) 15.2125,
(20) 15.3117, (28) 15.3905, $I_1 = 15.756 \text{ eV}$

Ar^+ : (6) 0.0000, (2) 13.4796, (20) 16.4151, (12) 16.7127,
(6) 17.1838, (28) 17.6921, (6) 18.0021, (12) 18.3058,
(10) 18.4422, (10) 18.5972, (12) 19.2369, (30) 19.6262,
(12) 19.9610, (2) 20.7432, (14) 21.1512, (26) 21.4488,
(38) 21.6719, (6) 22.2749, (40) 22.6886, (60) 23.0605,
(62) 23.5813, (34) 23.8292, (120) 24.0524, (84) 24.3003,
(48) 24.7963, (18) 25.4162, (6) 25.8616, (220) 26.0361,
(50) 26.6560, (70) 27.2759, $I_2 = 27.620 \text{ eV}$

Ar^{2+} : (5) 0.0000, (3) .1379, (1) .1947, (5) 1.7370, (1) 4.1245,
(9) 14.1835, (10) 15.8696, (28) 17.9339, (15) 19.4589,
(5) 21.6192, (1) 22.5646, (75) 23.4945, (15) 24.3747,
(5) 24.7963, (18) 25.3790, (21) 25.8253, (27) 26.1353,
(33) 26.5940, (46) 27.8338, (9) 28.7017, (5) 29.1356,

Table 3.1 (continued)

FR-126

Ar^{2+} : (26) 29.7555, (50) 30.5039, (91) 31.1193, (24) 31.9872,
(cont'd) (127) 33.4750, (121) 34.5288, (116) 34.9627,
(111) 35.4587, (524) 37.4424, $I_3 = 40.902 \text{ eV}$

Ar^{3+} : (4) 0.0000, (4) 2.6148, (6) 2.6308, (2) 4.3212,
(4) 4.3437, (6) 14.5757, (4) 14.6936, (2) 14.7592,
(4) 18.0915, (6) 18.1013, (4) 20.6250, (2) 20.7599,
(2) 22.0480, (12) 31.1596, (6) 31.8545, (10) 33.2467,
(20) 35.5690, (12) 35.8948, (10) 36.0913, (4) 36.1714,
(6) 36.6691, (2) 37.1402, (14) 37.7226, (10) 37.9711,
 $I_4 = 59.792 \text{ eV}$

Ar^{4+} : (1) 0.0000, (3) .0948, (5) .2519, (5) 2.0212, (15)
15.0922, (9) 17.5768, (3) 23.7470, (3) 24.2205,
(9) 27.0195, (15) 27.8395, (9) 36.8356, (3) 37.3556,
 $I_5 = 75.002 \text{ eV}$

Ar^{5+} : (2) 0.0000, (4) .2740, (2) 12.3981, (4) 12.4976,
(6) 12.6503, (2) 21.0522, (2) 22.5872, (4) 22.7601,
(10) 27.1053, (4) 33.5191, (12) 39.2509, (20) 39.6212,
(2) 42.4371, (10) 56.3853, (12) 56.4472, (10) 68.8673,
 $I_6 = 91.303 \text{ eV}$

Ar^{6+} : (1) 0.0000, (9) 14.2261, (3) 21.1661, (9) 33.6804,
(15) 40.1887, (3) 63.7367, (3) 70.2183, (15) 78.6846,
(21) 81.8391, (15) 95.7550, $I_7 = 124.007 \text{ eV}$

Table 3.1 (continued)

FR-126

Ar^{7+} :	(2) 0.0000, (6) 17.5892, (10) 41.2445, (2) 71.4021, (6) 77.9725, (10) 86.4791, (14) 88.8744, (2) 100.7280, (6) 103.2200, (10) 107.2560, (14) 108.5170, (10) 118.4720, $I_8 = 143.464 \text{ eV}$
Ar^{8+} :	(1) 0.0000, (8) 252.0970, (4) 254.4220, $I_9 = 421.000 \text{ eV}$
Ar^{9+} :	(4) 0.0000

Also calculated (as functions of P_e and T) were the following length scales useful for characterizing the plasma: The Debye lengths (D_0 , D_1); average impact parameter for 90° scattering (\bar{b}_0); the electron deBroglie wavelength (λ_e); and average interelectron and interionic separations (r_e and r_i). From these length scales, it was possible to obtain a dimensionless parameter QNTM ($=\lambda_e/D$) indicating the relative importance of quantum mechanical diffraction effects; and another parameter DGN ($=\lambda_e/r_e$) representing the electron degeneracy effects. Also calculated was INTPAR, the interaction parameter indicating the importance of classical non-ideal effects.

Finally, we calculated the electrical conductivity of the plasma using two approaches: Rogov [Reference 3.6 and Equation (3.55)] and Spitzer-Harm [Reference 3.5 and Equation (3.58)].

These calculated results were re-expressed as functions of (P , e) using a double-interpolation procedure. They were then conveniently presented in the form of Mollier charts. In Figures 3.2 through 3.3, we have presented excerpts from the argon Mollier chart data.

The purpose of Figure 3.2 is to elucidate the regimes where classical non-ideal, quantum diffraction, and electron degeneracy effects play an important role. These results were calculated on the basis of the Debye-Huckel theory with no ion participation (DHO).

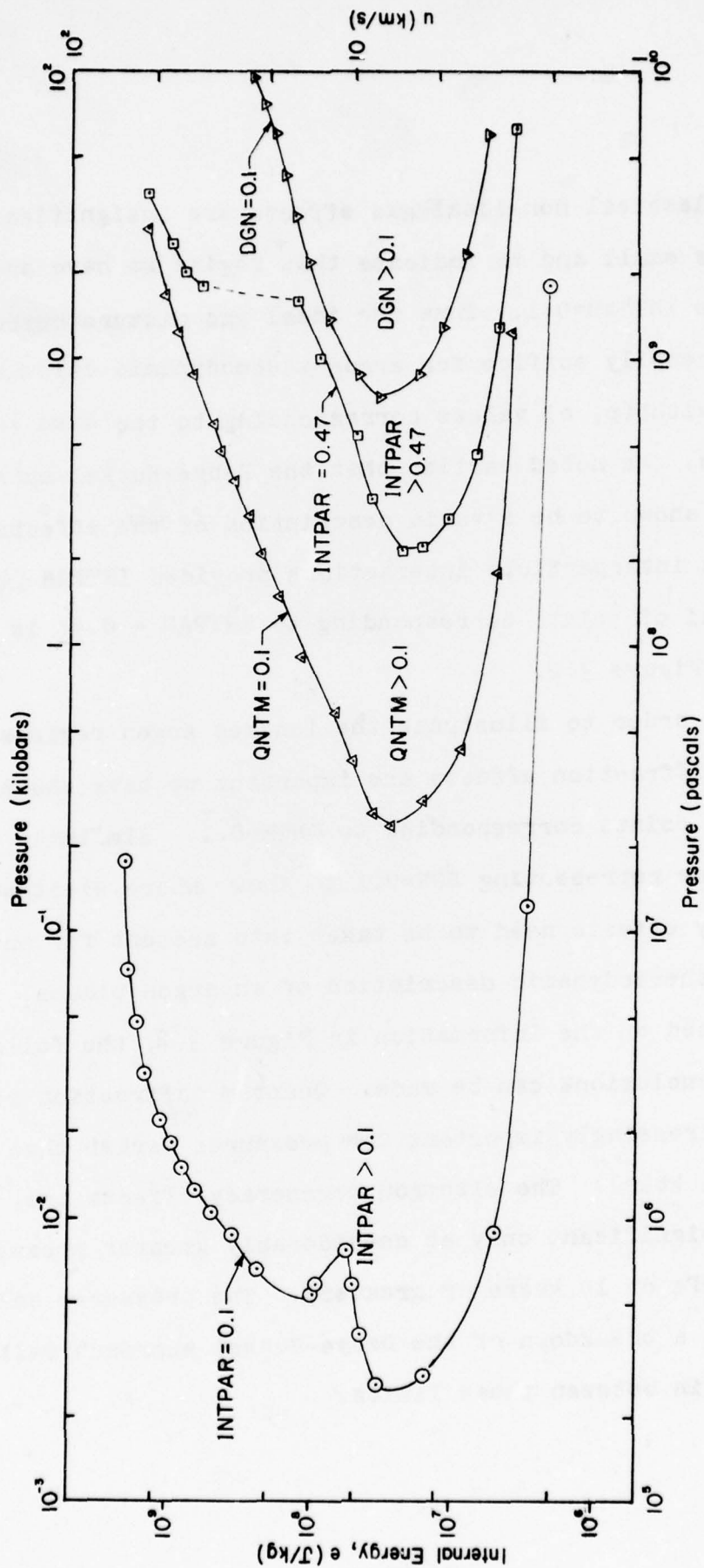


Figure 3.2 Argon: Lines of Constant Interaction Parameter, Quantum Collisional Effects Parameter (QNTM) and Electron Degeneracy Parameter (DGN) - Based on Debye-Huckel Thermodynamics (DHO).

Classical non-ideal gas effects are insignificant when $INTPAR$ is small and to indicate this regime we have shown a line with $INTPAR=0.1$. Thus our ideal gas mixture approach would generally suffice for argon thermodynamic calculations for plasmas with (p, e) values corresponding to the area left of this line. We noted earlier that the Debye-Huckel approach has been shown to be a valid description of the effects of coulombic interparticle interactions provided $INTPAR \leq 0.47$. The loci of points corresponding to $INTPAR = 0.47$ is also shown in Figure 3.2.

In order to illustrate the ionized argon regimes where quantum diffraction effects are important we have shown the loci of points corresponding to $QNTM=0.1$. Similarly we have a line representing $DGN=0.1$ to show where electron degeneracy effects need to be taken into account for an accurate thermodynamic description of an argon plasma.

Based on the information in Figure 3.2, the following general conclusions can be made. Quantum diffraction effects become increasingly important for pressures larger than about 100 MPa (1 kbar). The electron degeneracy effects are, however, significant only at considerably greater pressures (about 1 GPa or 10 kbars or greater). The pressures corresponding to a breakdown of the Debye-Huckel approach fall somewhere in between these limits.

In Figure 3.3, we have shown a Mollier chart for argon showing lines of constant mass density (ρ), specific dimensionless entropy (s/R) and enthalpy (h). These calculations were also performed using the DHO approach and the reliability of the results naturally depends upon the relative importance of the classical non-ideality, electron degeneracy and quantum diffraction effects as indicated by Figure 3.2.

Figure 3.4 shows a Mollier chart for electrical conductivity calculated on the basis of the asymptotic limit of Rogov's theory and DHO equilibrium thermodynamics. Lines of constant conductivity are given from 6KS/m (60 mho/cm) up to 100 KS/m (1000 mho/cm).

3.5 Xenon Calculations

In carrying out equation of state calculations for xenon, we were plagued with a major problem right at the outset--the lack of adequate ionization potential and electronic energy level data. Unlike the case for argon, Charlotte Moore's compilation (Reference 3.8) of the xenon data extends to only Xe^{3+} . This is far too limited to be useful for calculations over the wide pressure and energy range of interest to us. Reference 3.9 provides ionization potential data up to Xe^{6+} but for reasons discussed later, there is some doubt about the accuracy of some of this data.

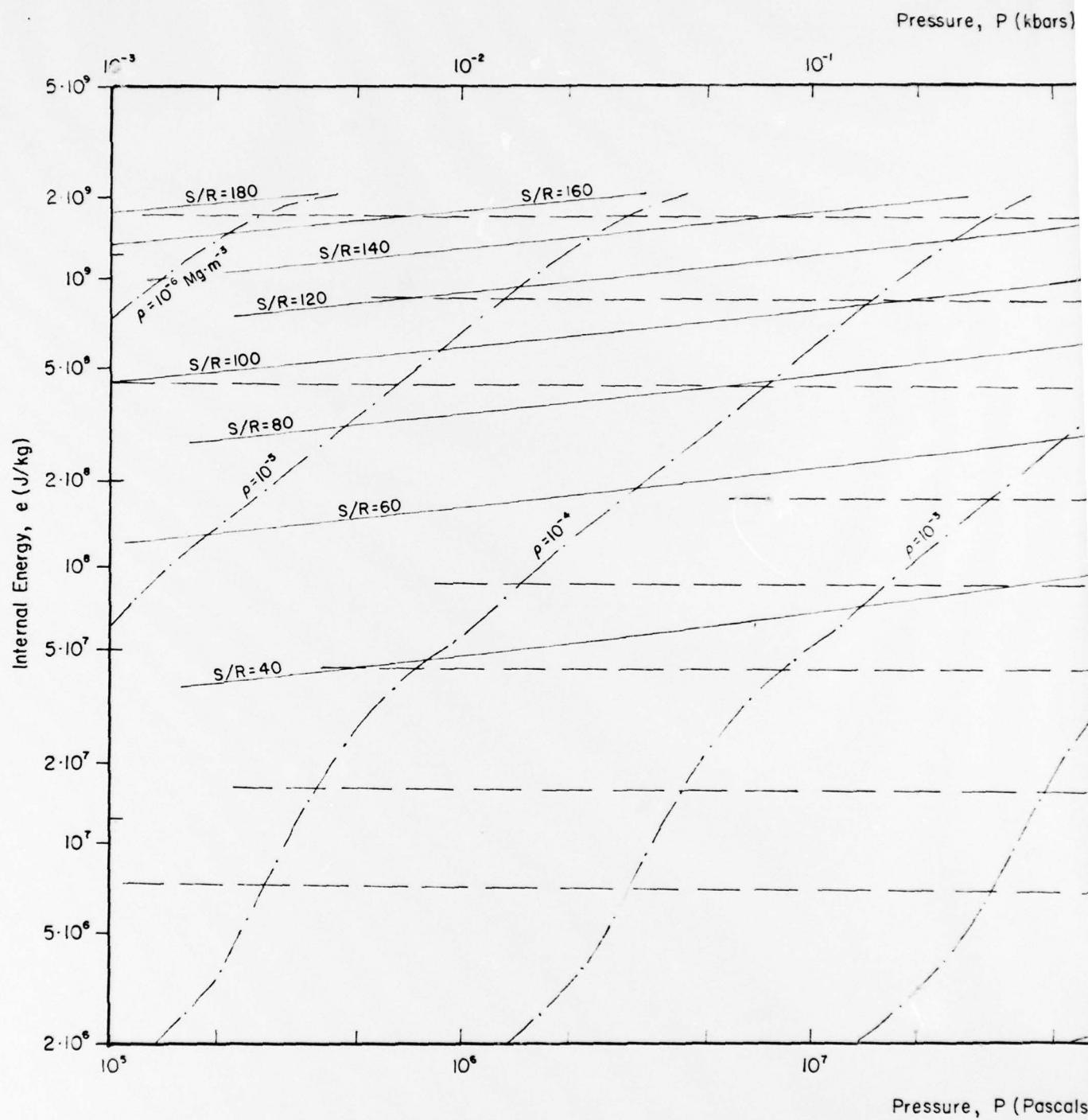
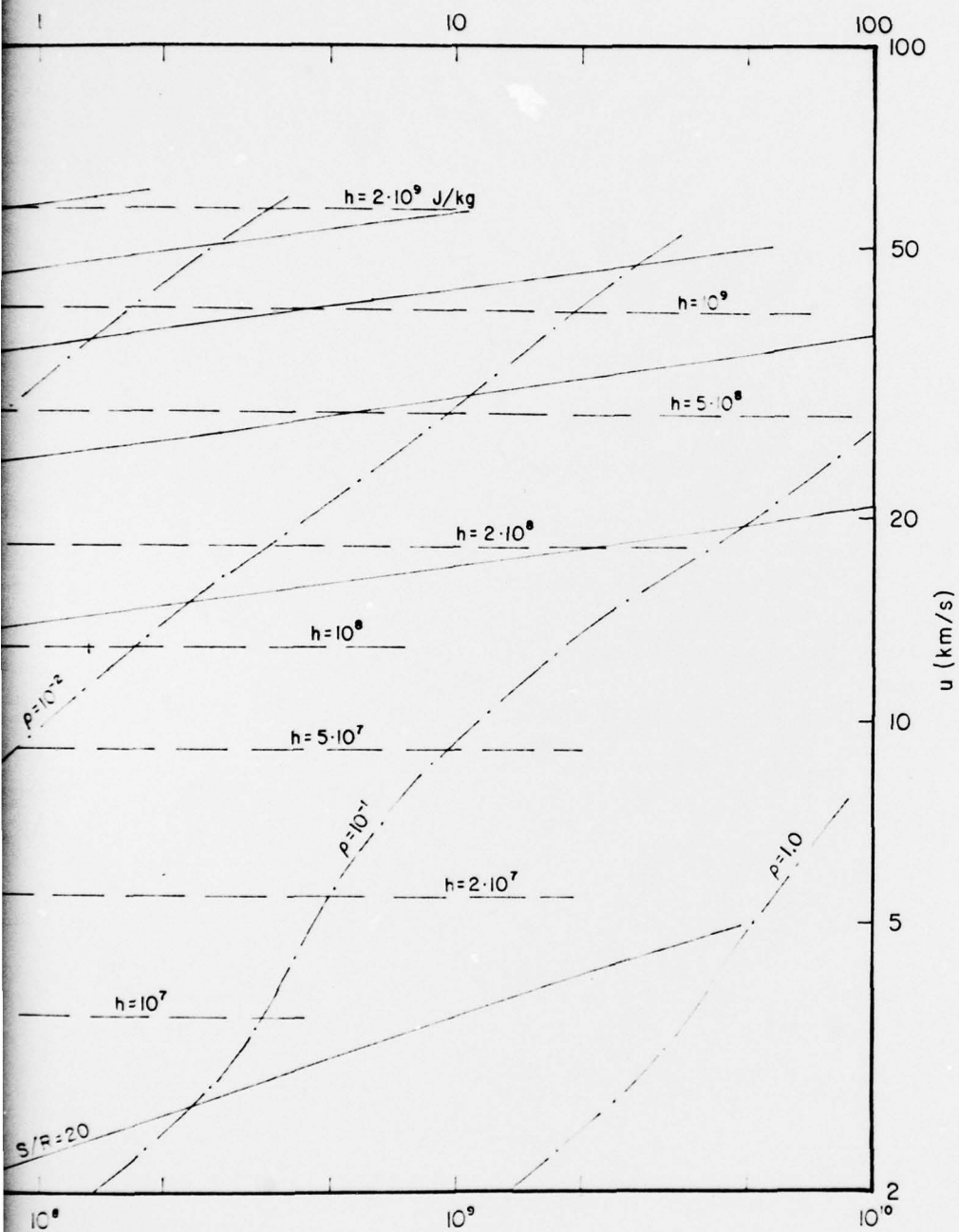


Figure 3.3 Argon: Mollier Chart for ρ ($\text{Mg} \cdot \text{m}^{-3}$), S/R and h (J/kg). Calculations



and on Modified Debye-Huckel Theory (DHO).

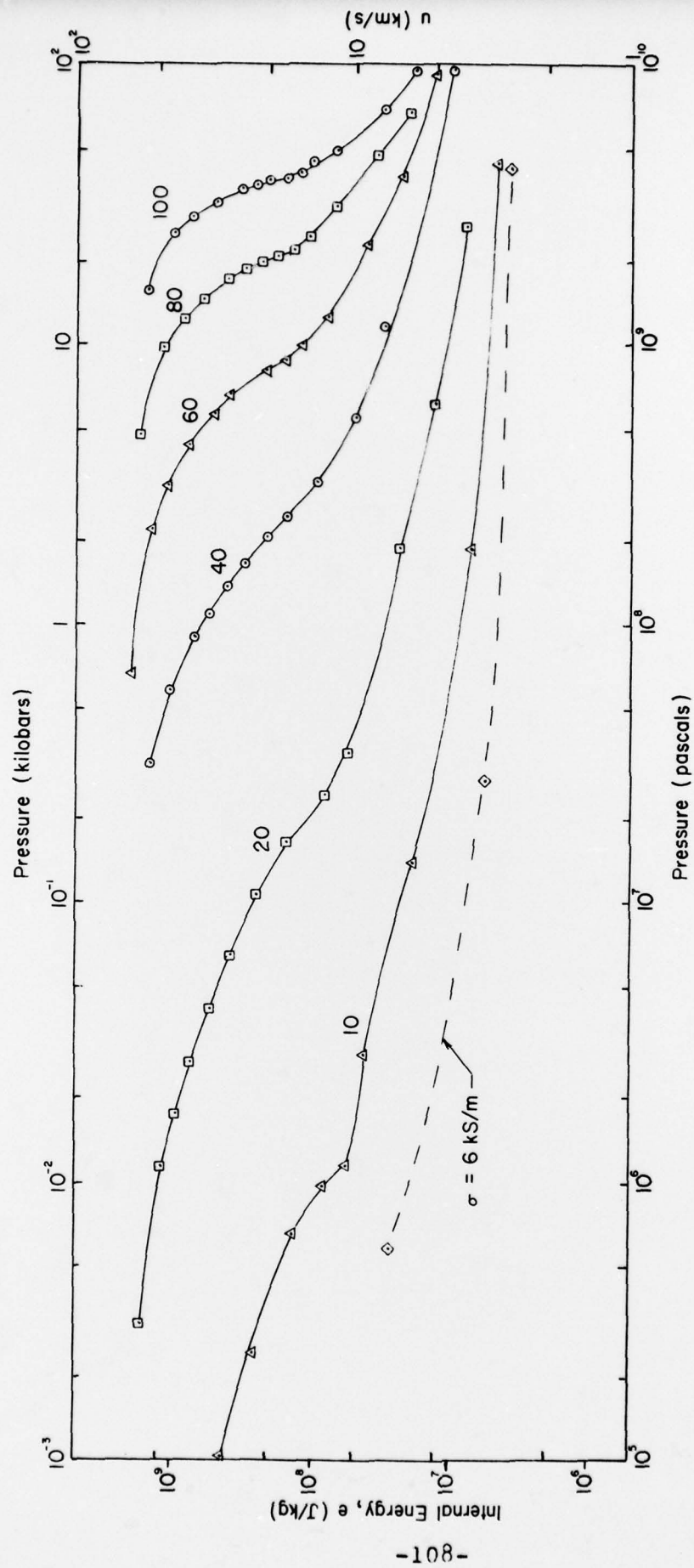


Figure 3.4 Argon: Mollier Chart for Electrical Conductivity Using Rogov's Asymptotic Expression and Debye-Huckel Thermodynamics (DHO).

For this reason our detailed calculational effort including the preparation of Mollier charts emphasized argon, for which adequate data had been available in Reference 3.8. The xenon calculations were intentionally kept limited in scope, pending the availability of more complete and reliable data. Table 3.2 shows the data used for the xenon calculations presented here and these are drawn from References 3.8 and 3.9. As in the case of argon, the individual electronic energy levels have been combined into groups, spread about an eV apart.

The xenon calculations were carried out for electron pressure (P_e) ranging from 1 MPa (10 bars) to 2 GPa (20 kbars) and at temperatures of 1, 2, 4, 6, 8, 10 and 20 eV. The results for the higher temperatures (8-20 eV) are particularly sensitive to the ionization potential data used and, in view of the uncertainties in such data, should be interpreted with caution. Calculations were based on three approaches: ideal gas, DHO and DH1 and the last of these displayed thermodynamic instabilities (characterized by calculated P 's becoming negative) beginning around the 4 eV, 1 GPa region.

In Figures 3.5 and 3.6 we have presented a segment of the xenon calculations based on the D-H approach. Because of doubts about the accuracy of the results, we have not carried out the double interpolation needed to express the calculated results in the Mollier chart form but have instead presented them as functions of P_e for constant values of T .

Table 3.2 IONIZATION POTENTIALS (I_m) AND ENERGY GROUPS (eV)
AND GROUP DEGENERACIES USED IN CALCULATION OF
EQUATION OF STATE OF XENON

Xe:	(1) 0.0000, (8) 8.3606, (68) 9.9190, (81) 10.9781, $I_1 = 12.127$ eV
Xe ⁺ :	(4) 0.0000, (2) 1.3064, (50) 11.9490, (48) 13.1310, (64) 14.1410, (42) 15.4400, (124) 16.7080, $I_2 = 21.200$ eV
Xe ²⁺ :	(5) 0.0000, (4) 1.1628, (5) 2.1201, (1) 4.6367, (8) 12.4290, (17) 13.8570, (45) 15.4240, (48) 16.6150, (55) 18.0770, (37) 19.1140, (66) 20.4240, (23) 21.7080, (55) 22.7220, $I_3 = 31.300$ eV
Xe ³⁺ :	(4) 0.0000, (10) 1.9607, (2) 3.4759, (4) 5.1927, (22) 12.8740, (14) 15.4310, (24) 16.7730, (24) 18.2320, (18) 19.6990, (32) 20.8810, (24) 21.9210, (10) 23.0670, $I_4 = 42.000$ eV
Xe ⁴⁺ :	(1) 0.0000, $I_5 = 53.000$ eV
Xe ⁵⁺ :	(1) 0.0000, $I_6 = 58.000$ eV
Xe ⁶⁺ :	(1) 0.0000, $I_7 = 135.000$
Xe ⁷⁺ :	(1) 0.0000

Figure 3.5 shows the dependence of the plasma interaction parameter (INTPAR), electrical conductivity (Rogov's method), Flowspeed (u) corresponding to strong shock compression [$u=(2e)^{1/2}$] the electron degeneracy parameter (DGN), average square charge (\bar{Z}^2) and an effective γ on P_e and at $T=116\text{ kK}$. Figure 3.6 shows the dependence of the pressure (P), mass density (ρ), electron number density (n_e) and the quantum diffraction parameter (QNTM) on P_e for T fixed at 116 kK (10 eV).

Following the completion of these xenon calculations, we were able to find sources of information about theoretical calculations of the ionization potentials of argon and xenon. Reference 3.7 contains a compilation of ionization potentials and somewhat limited electronic energy levels recently calculated by standard quantum chemistry techniques. In Table 3.3 we have compared the calculated ionization potentials for argon and xenon (the "FRAGA" column) with the measured values obtained from Reference 3.8 (the "Moore" column) and 3.9 (the "HCP" column). Very recently we were able to obtain a preprint of argon spectroscopic data that are being compiled under the leadership of Professor John Stoner at the University of Arizona. This revised argon data is not only more complete than the older data in Reference 3.8 but also extends to very high ionicities. This data is shown under the column labelled "Stoner" for argon. As far as xenon is concerned,

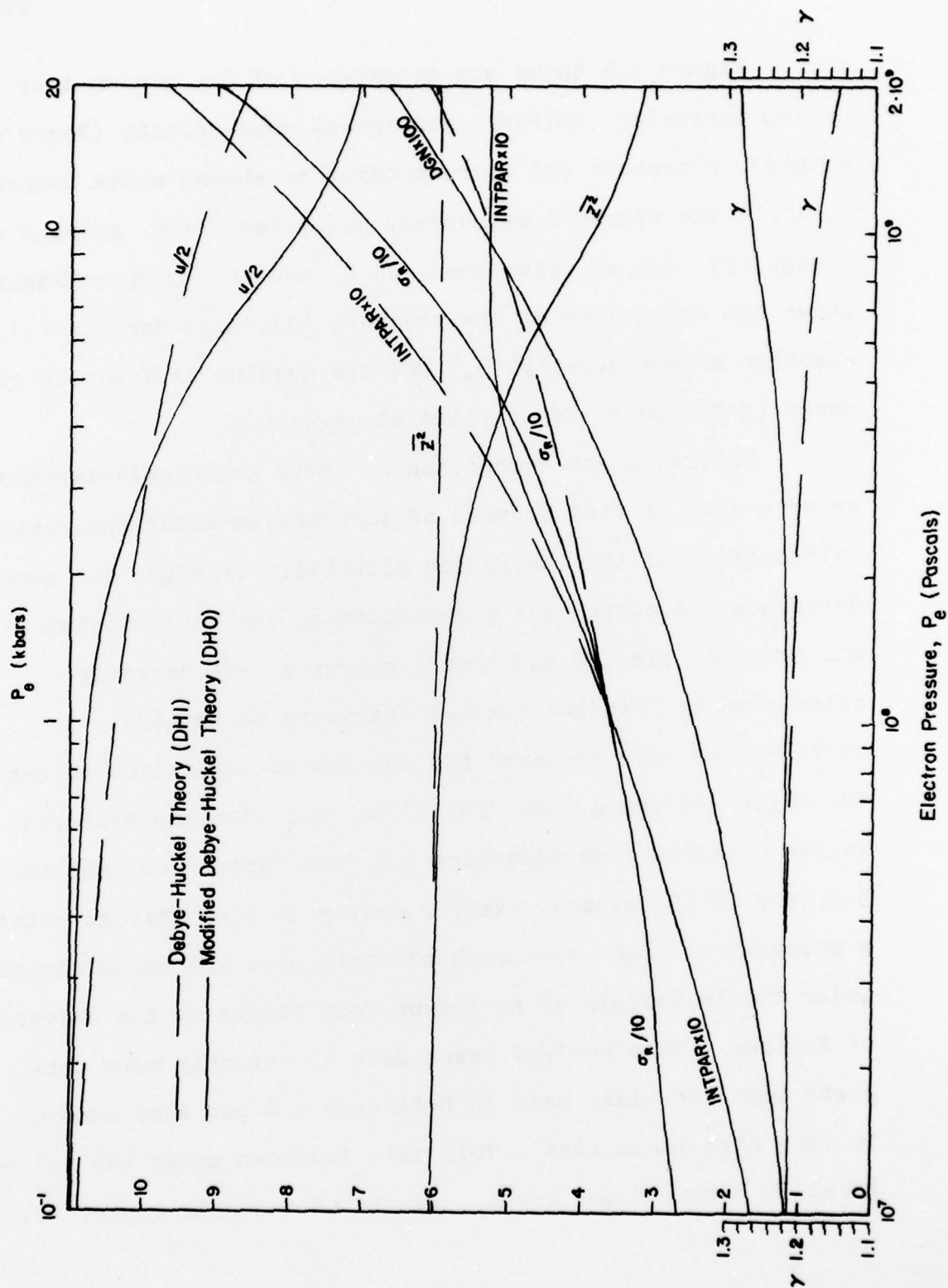


Figure 3.5 Xenon, $T=10\text{ eV}$: Dependence of INTPAR, σ_e ($\text{kS}\cdot\text{m}^{-1}$), u ($\text{km}\cdot\text{s}^{-1}$), DGN, γ and z^2 on P_e .

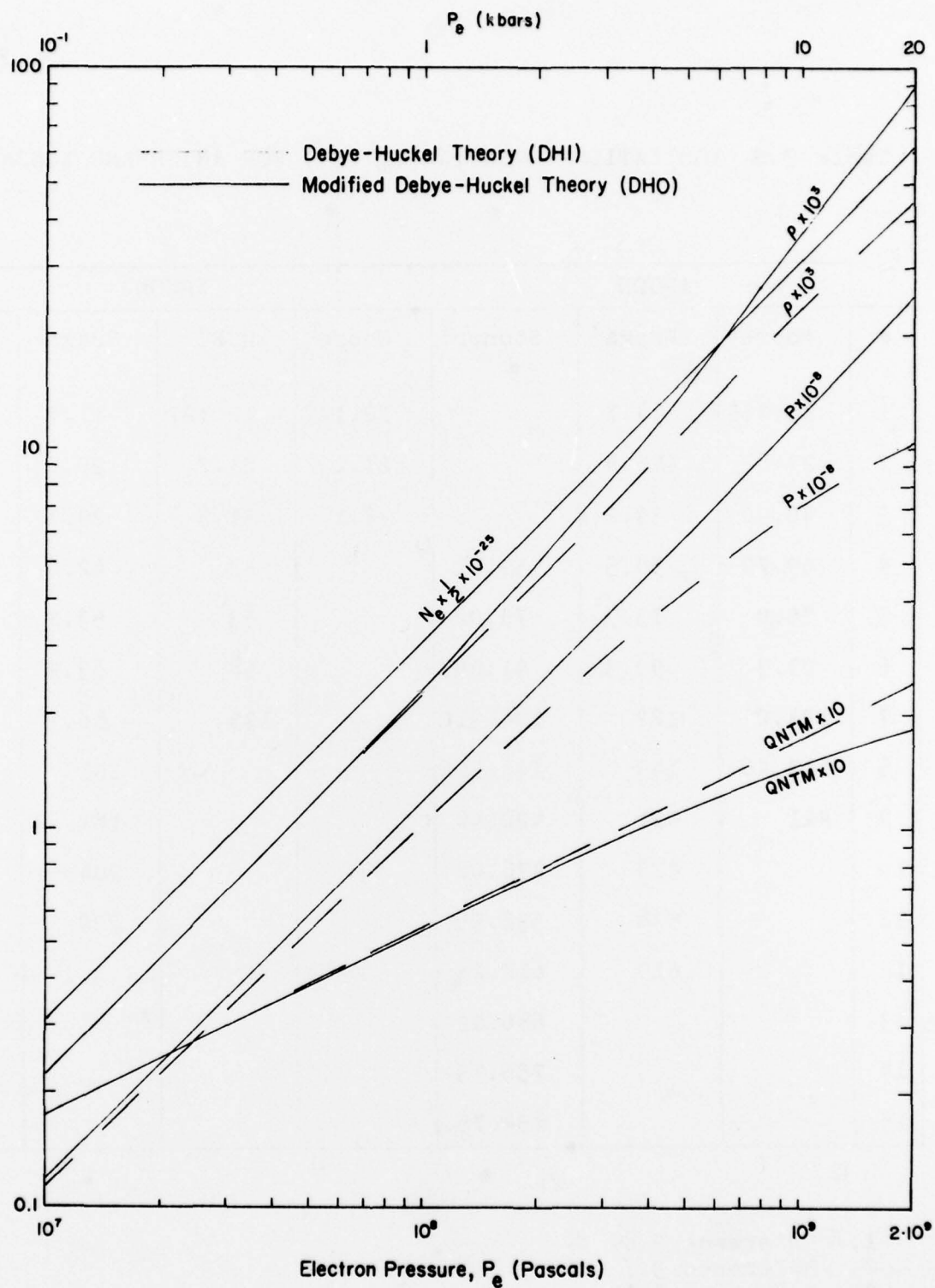


Figure 3.6 Xenon, $T=10$ eV: Dependence of ρ ($\text{Mg}\cdot\text{m}^{-3}$), N_e (m^{-3}), P (Pa), and QNTM on P_e .

Table 3.3 IONIZATION POTENTIAL I_m (eV) FOR ARGON AND XENON

m	ARGON			XENON			
	Moore ¹	Fraga ²	Stoner ³	Moore ¹	HCP ⁴	Fraga ²	Kim ⁵
1	15.755	14.7		12.127	12.127	11.7	11.27
2	27.62	26.4		21.2	21.2	20.0	20.41
3	40.90	39.2		32.1	31.3	29.1	30.40
4	59.79	58.5	59.81		42	42.6	40.92
5	75.0	73.9	75.02		53	53.2	53.25
6	91.3	90.3	91.007		58	63.9	65.69
7	124.0	122	124.319		135	86.7	89.61
8	143.46	143	143.406			101	104.3
9	421	421	422.44			181	178.2
10		478	478.68			204	203.2
11		538	538.95			230	228.9
12		619	618.24				255.4
13			686.09				282.7
14			755.73				310.7
15			854.75				

1. Reference 3.8
2. Reference 3.7
3. Reference 3.12
4. Reference 3.9
5. Reference 3.10

we were fortunate that Dr. Yong-Ki Kim of the Argonne National Laboratories was kind enough to perform a Hartree-Fock molecular orbital calculation for us. Dr. Kim's results for xenon ionization potentials are also shown in Table 3.3.

A careful reading of Table 3.3 indicates that the new data for argon are not very different from those used in the calculations reported in Section 3.4 and hence those results are expected to be valid within the context of the Debye-Huckel treatment and the neglect of quantum mechanical diffraction and degeneracy effects. The situation is very different for xenon, however. We note, in particular, a glaring discrepancy in I_7 for xenon between the measured value of 135 eV reported in Reference 3.9 ("HCP") and the calculated values of 86.7 and 89.61 obtained by Fraga (Reference 3.7) and Dr. Kim, respectively.

4. RESULTS AND RECOMMENDATIONS

4.1 Program Accomplishments

- 1) Advanced concepts for increasing the performance of explosive xenon plasma sources were developed and tested experimentally.
- 2) Plasma diagnostic data was successfully obtained using MHD velocity gages, plasma conductivity gages, plasma resistance measurements, and shock wave instrumentation.
- 3) The best performance was obtained with an unphased symmetric disc plasma source. The peak plasma velocity of 29 km/s represents a 45% increase over the best performance last year.
- 4) It was determined that phasing concepts for increasing plasma source performance did not work as expected, and a tentative hypothesis explaining the observed data was developed.
- 5) A computer code was developed to perform non-ideal plasma calculations using the best available theory.
- 6) A full range of calculations were performed to generate an argon Mollier chart in the region of experimental

interest. Some calculations were performed for xenon, but they were limited by a lack of data at high ionicity.

4.2 Recommendations

- 1) Additional research to increase the performance of explosive plasma sources is required for useful self-excited MHD pulse generators. The best plasma source in this program yields an 18 dB magnetic field gain, and a gain of 44 dB is a reasonable criterion for a practical generator using permanent magnets. This goal could be achieved at the present 20 μ s pulse duration by increasing average velocity to 24 km/s, or by increasing pulse duration to 43 μ s at the present 14 km/s average velocity, or a combination. Increasing the plasma conductivity will also help, but not as much as velocity and pulse duration, since present performance is high enough to reduce the influence of conductivity on magnetic field gains.
- 2) The non-ideal argon plasma calculations should be compiled and published for wide distribution.
- 3) The xenon calculations should be extended with best available theoretical estimates of ionization potentials and published.

REFERENCES

- 1.1 Gill, S.P., et al, "Explosive MHD Research", Artec Associates Incorporated Final Report 119, Navy Contract N00014-75-C-0822.
- 1.2 Gill, S.P., et al, "Explosive MHD Research", Artec Associates Incorporated Annual Report 119AR, Navy Contract N00014-75-C-0822, April 1976.
- 1.3 Baum, D.W., et al, "Development of High Energy Density Simulator", Artec Associates Incorporated Final Report 120, Defense Nuclear Agency Contract DNA001-75-C-0271, December 1976.
- 3.1 Gill, S.P., et al, "Explosive MHD Research", Artec Associates Incorporated Final Report 119, Navy Contract N00014-75-C-0822.
- 3.2 Zel'dovich, Ya.B., and Raizer, Yu.P., "Physics of Shock Waves and High-Temperature Hydrodynamic Phenomena", Vol. I, Academic, N.Y., 1966.
- 3.3 Berlin, T.H., and Montroll, E.W., J. Chem. Phys., 20, 1952. p. 75.
- 3.4 Griem, H.R., "High Density Corrections in Plasma Spectroscopy", Phys. Rev., 128, 1962, p. 997.
- 3.5 Spitzer, L., "Physics of Fully Ionized Gases", Wiley Interscience, 2nd. Edition, 1962.
- 3.6 Rogoff, V.S., "Calculation of Plasma Conductivity", Tepl. Vys. Temp., 8, 1970, p. 689.
- 3.7 Fraga et al, "Handbook of Atomic Data", Elsevier--North Holland, N.Y., 1976.
- 3.8 Moore, C.E., "Atomic Energy Levels", NBS Circ. 467, U.S. Dept. Commerce, 1949.
- 3.9 "Handbook of Chemistry and Physics", 50th Ed., Chemical Rubber Publishing Company.

- 3.10 Kim, Yong-Ki, private communication.
- 3.11 Miller, C.G., and Wilder, S.E., "Tables and Charts of Equilibrium Normal Shock and Shock Tube Properties for Pure Argon with Velocities to 10 km/sec", NASA SP-3098, 1976.
- 3.12 Stoner, J., private communication.
- 3.13 Gilmore, F.R., "Thermal Radiation Phenomena", Vol. I, DASA 1971-1, May 1967.